The Astrophysical Journal, 752:46 (23pp), 2012 June 10 doi:10.1088/0004-637X/752/1/46

THE 4 Ms *CHANDRA* DEEP FIELD-SOUTH NUMBER COUNTS APPORTIONED BY SOURCE CLASS: PERVASIVE ACTIVE GALACTIC NUCLEI AND THE ASCENT OF NORMAL GALAXIES

B. D. Lehmer[1,2], Y. Q. Xue[3,4], W. N. Brandt[3,4], D. M. Alexander[5], F. E. Bauer[6], M. Brusa[7], A. Comastri[8], R. Gilli[8], A. E. Hornschemeier[2], B. Luo[9], M. Paolillo[10], A. Ptak[2], O. Shemmer[11], D. P. Schneider[3,4], P. Tozzi[12], and C. Vignali[13]

[1] The Johns Hopkins University, Homewood Campus, Baltimore, MD 21218, USA
[2] NASA Goddard Space Flight Centre, Code 662, Greenbelt, MD 20771, USA
[3] Department of Astronomy and Astrophysics, Pennsylvania State University, University Park, PA 16802, USA
[4] Institute for Gravitation and the Cosmos, Pennsylvania State University, University Park, PA 16802, USA
[5] Department of Physics, Durham University, Durham DH1 3LE, UK
[6] Departamento de Astronomia y Astrofisica, Pontificia Universidad Catolica de Chile, Casilla 306, Santiago 22, Chile
[7] Max-Planck-Institut für Extraterrestrische Physik, Giessenbachstrasse, D-85748 Garching, Germany
[8] INAF-Osservatorio Astronomico di Bologna, Via Ranzani 1, I-40127 Bologna, Italy
[9] Harvard-Smithsonian Center for Astrophysics, 60 Garden Street, Cambridge, MA 02138, USA
[10] Dipartimento di Scienze Fisiche, Universitá Federico II di Napoli, Via Cinthia, I-80126 Napoli, Italy
[11] Department of Physics, University of North Texas, Denton, TX 76203, USA
[12] INAF-Osservatorio Astronomico di Trieste, Via Tiepolo 11, I-34131 Trieste, Italy
[13] Dipartimento di Astronomia, Universitá di Bologna, Via Ranzani 1, I-40127 Bologna, Italy
Received 2012 February 10; accepted 2012 April 9; published 2012 May 24

ABSTRACT

We present 0.5–2 keV, 2–8 keV, 4–8 keV, and 0.5–8 keV (hereafter soft, hard, ultra-hard, and full bands, respectively) cumulative and differential number-count (log N–log S) measurements for the recently completed ≈4 Ms *Chandra* Deep Field-South (CDF-S) survey, the deepest X-ray survey to date. We implement a new Bayesian approach, which allows reliable calculation of number counts down to flux limits that are factors of ≈1.9–4.3 times fainter than the previously deepest number-count investigations. In the soft band (SB), the most sensitive bandpass in our analysis, the ≈4 Ms CDF-S reaches a maximum source density of ≈27,800 deg^{-2}. By virtue of the exquisite X-ray and multiwavelength data available in the CDF-S, we are able to measure the number counts from a variety of source populations (active galactic nuclei (AGNs), normal galaxies, and Galactic stars) and subpopulations (as a function of redshift, AGN absorption, luminosity, and galaxy morphology) and test models that describe their evolution. We find that AGNs still dominate the X-ray number counts down to the faintest flux levels for all bands and reach a limiting SB source density of ≈14,900 deg^{-2}, the highest reliable AGN source density measured at any wavelength. We find that the normal-galaxy counts rise rapidly near the flux limits and, at the limiting SB flux, reach source densities of ≈12,700 deg^{-2} and make up 46% ± 5% of the total number counts. The rapid rise of the galaxy counts toward faint fluxes, as well as significant normal-galaxy contributions to the overall number counts, indicates that normal galaxies will overtake AGNs just below the ≈4 Ms SB flux limit and will provide a numerically significant new X-ray source population in future surveys that reach below the ≈4 Ms sensitivity limit. We show that a future ≈10 Ms CDF-S would allow for a significant increase in X-ray-detected sources, with many of the new sources being cosmologically distant ($z \gtrsim 0.6$) normal galaxies.

Key words: cosmology: observations – galaxies: active – galaxies: starburst – X-rays: galaxies

Online-only material: color figures, Supplemental data file (tar.gz)

1. INTRODUCTION

Deep extragalactic X-ray surveys conducted with *Chandra* and *XMM-Newton* have resolved the vast majority of the 0.5–10 keV cosmic X-ray background (CXRB) and have provided substantial new insight into the X-ray point sources detected (see, e.g., Brandt & Hasinger 2005; Brandt & Alexander 2010). A fundamental quantity used to characterize the extragalactic X-ray source population is the cumulative X-ray number counts, which quantify how the cumulative number of X-ray sources per unit area, N, increases with decreasing flux, S (also referred to as log N–log S; see, e.g., Brandt et al. 2001; Rosati et al. 2002; Moretti et al. 2003; Bauer et al. 2004; Kim et al. 2007; Georgakakis et al. 2008). The number counts provide an observational constraint that must be considered when constructing physical models that describe the X-ray evolution of extragalactic sources in the universe. For example, successful models including the supermassive black hole (SMBH) accretion history of the universe (e.g., Gilli et al. 2007; Treister et al. 2009) and the X-ray evolution of normal galaxies (primarily driven by X-ray binaries and hot gas; see, e.g., Ranalli et al. 2003, 2005) must predict X-ray source densities consistent with the observed number counts.

Due to its high angular resolution and low background, *Chandra* is the only current X-ray observatory capable of providing new constraining data in the ultra-deep regime (below 0.5–8 keV fluxes of a few $\times 10^{-16}$ erg cm^{-2} s^{-1}), since the deepest *Chandra* surveys have now greatly surpassed the *XMM-Newton* confusion limit (see, e.g., Brandt et al. 2001; Giacconi et al. 2001, 2002; Alexander et al. 2003; Luo et al. 2008; Xue et al. 2011). As new *Chandra* surveys continue to probe the extragalactic X-ray universe to fainter depths, the number counts continuously rise as fainter X-ray populations are revealed. Naturally, it is at the faintest flux levels where ultra-deep *Chandra* surveys are probing new regions of discovery space and classes of extragalactic sources that were poorly sampled at X-ray energies in the past (e.g., star-forming and passive galaxies, and obscured and low-luminosity active galactic nuclei (AGNs)).

Bauer et al. (2004; hereafter B04) measured the number counts for X-ray point sources detected in the ≈2 Ms *Chandra* Deep Field-North (CDF-N) and ≈1 Ms CDF-South (CDF-S),

the deepest *Chandra* surveys at the time. Using the available multiwavelength data, B04 were able to distinguish between different X-ray-emitting populations (e.g., AGNs, normal galaxies, and Galactic stars) and measure their contributions to the CXRB. B04 found that, generally, AGNs make up exclusively the relatively bright number counts. However, at the faintest flux levels in the 0.5–2 keV bandpass, the most sensitive bandpass studied in the CDF surveys, B04 showed that normal galaxies start to compose an appreciable fraction of the number counts ($\approx$25% of sources with $S_{0.5-2\,\mathrm{keV}} \approx (2\text{–}10) \times 10^{-17}$ erg cm^{-2} s^{-1}).

Recently, the deepest extragalactic X-ray survey yet conducted, the CDF-S, has reached a total exposure of $\approx$4 Ms (Xue et al. 2011, hereafter X11). X11 presented point-source catalogs and data products for the survey and provided basic multiwavelength classifications for the 740 individually detected X-ray sources in their main catalog. This work has revealed that, at the faintest flux levels, normal galaxies are playing an increasingly important role in the new sources detected. For example, at 0.5–2 keV fluxes below $\approx 5 \times 10^{-17}$ erg cm^{-2} s^{-1}, $\approx$50% of the X-ray-detected sources are classified as likely normal galaxies; below the current detection limits, it is almost certain that the normal-galaxy fraction continues to increase (e.g., B04; Ranalli et al. 2005).

In this paper, we present number counts for the new $\approx$4 Ms CDF-S, focusing on the faint-flux regime (0.5–2 keV fluxes $\lesssim 10^{-17}$ erg cm^{-2} s^{-1}). In Section 2, we describe a new Bayesian method for computing number counts, which properly accounts for biases and measurement uncertainties that are present in the important flux regime near the detection limit. In Section 3, we utilize the available multiwavelength photometric data as well as optical spectroscopic and photometric redshift catalogs to quantify, with good reliability, the relative contributions to the number counts from AGNs, normal galaxies, and Galactic stars. We further break down the number counts to quantify the contributions that subpopulations make to the AGN (with redshift, intrinsic AGN column density, and X-ray luminosity subpopulations) and normal galaxy (with redshift and morphological subpopulations) number counts. We conclude Section 3 by discussing how each population and subpopulation contributes to the overall CXRB intensity. In Section 4, we use our subpopulation number-count estimates to compare with predictions from phenomenological models that describe how the X-ray emission from accreting SMBHs and normal galaxies are expected to evolve with cosmic time. In Section 5, we use these models to estimate directly number counts to flux levels below current detection limits and highlight the prospects of deeper X-ray surveys. In Section 6, we summarize our findings.

Throughout this paper, we make use of the main point-source catalog and data products provided by X11. The Galactic column density for the CDF-S is 8.8×10^{19} cm^{-2} (Stark et al. 1992). All of the X-ray fluxes and luminosities quoted throughout this paper have been corrected for Galactic absorption. In the X-ray band, we make use of four bandpasses: 0.5–2 keV (soft band (SB)), 2–8 keV (hard band (HB)), 4–8 keV (ultra-hard band (UHB)), and 0.5–8 keV (full band (FB)). Values of $H_0 = 70$ km s^{-1} Mpc^{-1}, $\Omega_{\mathrm{M}} = 0.3$, and $\Omega_{\Lambda} = 0.7$ are adopted throughout this paper (e.g., Spergel et al. 2003).

2. METHODOLOGY FOR COMPUTING NUMBER COUNTS

Our primary goal is to evaluate the number counts across the entire $\approx$465 arcmin^2 $\approx$4 Ms CDF-S to the faintest possible flux levels. In the faint-flux regime, computing number counts presents a challenge, since these calculations must properly account for (1) the non-negligible spatial variations in sensitivity across the *Chandra* image, (2) incompleteness issues related to source-detection algorithms (see Section 2.1), and (3) the Eddington bias. The B04 investigation of the CDF number counts implemented Monte Carlo simulations using an extrapolated faint-flux number-count model to measure and correct for these biases. Although this method provides reasonable first-order corrections that account for the biases near the flux limits, it does not optimize the input faint-flux model. Such an optimization would require several Monte Carlo runs with varying faint-flux extrapolations, which is not feasible due to the computational requirements of this procedure. Such a limitation will therefore introduce small systematic errors in the number-count measurements near the flux limit if the wrong faint-end number-count prior is chosen.

To mitigate this difficulty, we employ an approach similar to the Poissonian-based methods described by Georgakakis et al. (2008, hereafter G08); however, our method has been adapted to account for the different source-detection methods adopted for the $\approx$4 Ms CDF-S catalog by X11. The X11 source-detection criteria make use of both `wavdetect` (Freeman et al. 2002) for initial source selection and `ACIS Extract` (`AE`) to improve photometry and re-evaluate source-detection significance (Broos et al. 2010). `AE` makes use of binomial statistics to evaluate source significance, and it properly accounts for point-spread function (PSF) variations between observations and uncertainties in local background measurements (see below). Our method for computing number counts, described in detail below, uses a Bayesian approach with maximum-likelihood optimizations to account for the Eddington bias and completeness limitations without requiring a large number of time-consuming simulations.

2.1. Source Recovery Functions and Flux Probability Distributions

Number-count computations at the flux limits depend sensitively on the solid angle of the survey over which a source of a given flux could be detected. As described in Section 3 of X11, to be included in the main catalog, an X-ray source must (1) be detected by `wavdetect` at a false-positive probability threshold of 10^{-5} and (2) contain s counts (derived from `AE`; see Columns 8–16 of Table 3 in X11) within an aperture representing $\approx$90% of the point-source encircled-energy fraction (EEF)[14] that satisfies the following binomial probability criterion:

$$P(x \geqslant s) = \sum_{x=s}^{n} \frac{n!}{x!(n-x)!} p^x (1-p)^{n-x} \leqslant P_{\mathrm{thresh}}, \qquad (1)$$

where $n \equiv s + b_{\mathrm{ext}}$ and $p \equiv 1/(1 + b_{\mathrm{ext}}/b_{\mathrm{src}})$. Here b_{ext} is the total number of background counts extracted from a large region outside of the point source (while masking out regions from other X-ray-detected sources) that was used to obtain an estimate of the local background count rate. The quantity b_{src} is the estimated number of background counts within the source extraction region, which was measured by rescaling

[14] As noted by X11, in special cases where sources had nearby neighbors, the source-detection probability was measured using an aperture smaller than the $\approx$90% EEF; however, only $\approx$2%–3% of all sources had moderate source crowding, where detection probabilities were measured using apertures that encompass $\lesssim$50% EEF. We therefore expect that this will have a negligible effect on our number-count measurements.

$b_{\rm ext}$ to the area of the source aperture (typically, $b_{\rm ext}/b_{\rm src} \approx 16$; see Section 4.1 of X11 for details). In Equation (1), $P_{\rm thresh} = 0.004$, the value adopted by X11. This choice of $P_{\rm thresh}$ was empirically selected both to optimize the number of sources detected and to ensure that nearly all detected sources are reliable (see Section 4.1 of X11). This multi-stage procedure for identifying a highly reliable list of source candidates will *not* result in a complete selection of *all* real sources in the image having binomial probabilities $\leqslant P_{\rm thresh}$, since the initial `wavdetect` selection has more complex source-detection criteria (see Freeman et al. 2002 for details) than the simple criterion given in Equation (1) (see Section 2.2 and the Appendix for discussion on correcting for these issues when computing number counts).

Using a probabilistic approach, we compute the solid angle of the sky within which a source with intrinsic flux S would be detected if present. First, using Equation (1), we define the quantity L, which is the number of counts required for a detection, which satisfies the relation $P(x \geqslant L) = P_{\rm thresh} = 0.004$. In order to compute L at each location in the CDF-S image, it is necessary to estimate local values of $b_{\rm src}$ and $b_{\rm ext}$ that are similar to those that would be estimated following the X11 approach used for the X-ray-detected sources. Unfortunately, the X11 procedure for extracting these values at every location in the image is computationally prohibitive, since source photometry is performed on an observation-by-observation basis (i.e., in up to 54 observations in total) and makes use of polygonal apertures that approximate local PSFs (see X11 for further details). To overcome this issue, we estimated $b_{\rm src}$ by extracting background counts from the merged CDF-S background maps (see Section 7.1 of X11) using circular apertures with sizes that encompass the 90% EEF for a point source. This approach was tested by comparing our $b_{\rm src}$ values measured in the regions of the X11 sources with those of X11. We find good agreement between values and a 1σ scatter at the $\approx$18%–25% level. To estimate appropriate values of $b_{\rm ext}$ at each location (pixel) on the CDF-S image, we measured the local off-axis angle θ_p; using the X11 point-source catalog, we adopted the maximum value of $b_{\rm ext}$ for sources with off-axis angles $\theta = \theta_p \pm 0.''25$. Given values of $b_{\rm src}$ and $b_{\rm ext}$, we numerically solved the relation $P(x \geqslant L) = 0.004$ to obtain L at each image location. In this manner, we constructed a spatial sensitivity map consisting of L values.

In principle, L could be combined with the exposure time to estimate a count-rate limit, which can in turn be converted to a single flux limit using a count-rate-to-flux conversion (as done in the X11 catalogs); however, this single flux-limit approach does not directly incorporate the probabilistic nature of source detection that is important in the low-count regime. It is therefore more informative to compute the probability that a source with intrinsic flux, S, would be detected given that L counts are required. Such a source is expected to contribute the following number of counts to the source-detection cell:

$$T = t_{\rm exp} C \eta S + b_{\rm src}, \tag{2}$$

where $t_{\rm exp}$, C, and η are the effective exposure time, the conversion from flux to count rate, and the EEF, respectively. Values of $t_{\rm exp}$ are taken directly from the exposure maps from X11 (see their Section 3.1). These exposure maps include the effects of vignetting, gaps between CCDs, bad-column filtering, bad-pixel filtering, and spatial and time-dependent degradation in quantum efficiency due to contamination on the ACIS optical-blocking filters. Values of C will depend on the spectral energy distribution (SED) shape. In this work we use power-law SEDs to characterize the observed spectra; these SEDs can be described using the photon index Γ. For each source, Γ was derived using the HB-to-SB count-rate ratio (corrected for differential vignetting and exposure times) as a proxy for spectral slope. The HB-to-SB count-rate ratio was calibrated against Γ using the AE-automated XSPEC-fitting procedure for relatively bright X-ray sources (with FB counts greater than 200; this ensures reliable XSPEC-fitting results). This approach takes into account the multi-epoch *Chandra* calibration information (see X11 for further details).

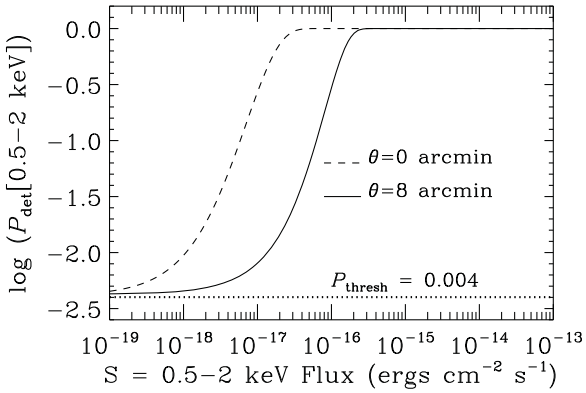

Figure 1. Detection probability as a function of intrinsic 0.5–2 keV flux for point sources located on axis (dashed curve) and $\approx 8'$ off axis (solid curve). These curves were computed considering a counts-to-flux conversion factor appropriate for a power-law SED with $\Gamma = 1.4$ (see Equations (2) and (3)), the mean photon index of the CXRB. Each curve asymptotes to the defined detection probability threshold $P_{\rm thresh} = 0.004$ (dotted line) at low flux levels. To construct the cumulative solid angle as a function of flux limit for the entire $\approx$4 Ms CDF-S image, we computed such curves at each location on the *Chandra* image multiplied by the effective solid angle per pixel ($\approx$0.242 arcsec^2) and added them (see Figure 2).

Therefore, at each location on the image, the probability of source detection as a function of flux S can be computed as follows:

$$P_{\rm det} = \sum_{x=L}^{L+b_{\rm ext}} \frac{(L+b_{\rm ext})!}{x!(L+b_{\rm ext}-x)!} \left(\frac{T}{T+b_{\rm ext}}\right)^x \times \left(1-\frac{T}{T+b_{\rm ext}}\right)^{L+b_{\rm ext}-x}, \tag{3}$$

where $b_{\rm ext}$ is the extracted background counts that were used to calculate the local background in Equation (1). Figure 1 shows $P_{\rm det}$ as a function of 0.5–2 keV flux $S_{0.5-2\,\rm keV}$ for randomly selected positions at $\theta \approx 0'$ and $8'$ offsets from the average aim point of the 4 Ms CDF-S (assuming $\eta = 0.9$ and a counts-to-flux conversion factor appropriate for a power-law SED with $\Gamma = 1.4$). We note that as the flux drops to zero, $P_{\rm det}$ asymptotically approaches our detection threshold $P_{\rm thresh} = 0.004$. This shows that, even when no source is present, there is still a finite (yet small, i.e., $P = 0.004$) probability that a positive fluctuation may exceed our adopted detection threshold; however, as shown by X11 through multiwavelength counterpart matching, the initial `wavdetect` source selection ensures that very few false sources are present in the X11 catalog.

We consider that each *Chandra* pixel represents a small local solid angle of size $d\Omega \approx 0.242$ arcsec^2 (i.e., $\approx 0.''492 \times 0.''492$) with a flux and SED (i.e., Γ) dependent detection probability distribution characterized by $P_{\rm det}$. Under this consideration, the total surveyed solid angle over which sources with flux S and

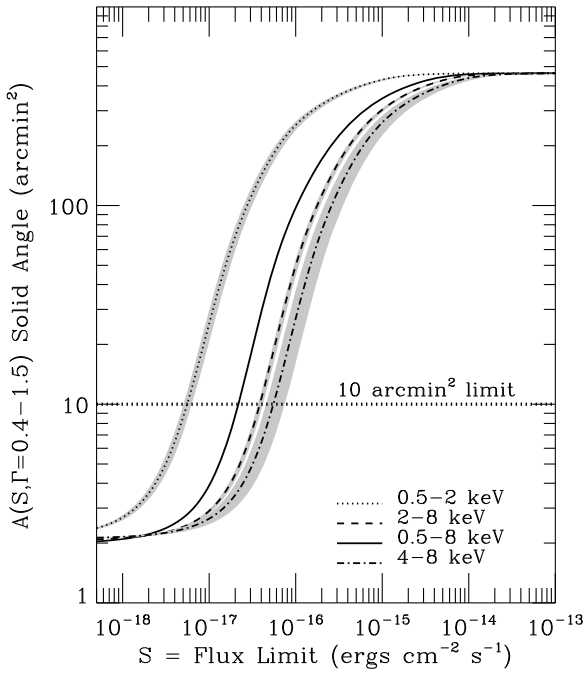

Figure 2. Effective solid angle $A(S)$ vs. intrinsic flux limit S for the SB (dotted curve), HB (short-dashed curve), UHB (dash-dotted curve), and FB (solid curve). These curves have been computed for a power-law SED with $\Gamma = 1.0$, the median photon index for sources detected in both the SB and HB. The shaded regions give the effective solid angle curves appropriate for the interquartile (≈25%–75%) range $\Gamma = 0.4$–1.5. These curves were computed following the probabilistic methods discussed in Section 2.1 and account for uncertainties in measured flux conversions at the lowest flux levels where the number of detected counts is small. The horizontal dotted line represents the ≈10 arcmin^2 limit, above which we can confidently compute number counts (see Section 2.1 for details). These curves are qualitatively different in nature from those produced by X11, which utilize single-valued count-rate-to-flux conversions.

photon index Γ could be detected when present is therefore $A(S, \Gamma) = \sum_i P_{\mathrm{det},i}\ d\Omega$ (hereafter the effective solid angle), where the summation is over all possible detection cells (i.e., all pixels). In Figure 2, we show $A(S, \Gamma = 1.0)$ versus S for the ≈4 Ms CDF-S in the four bandpasses. The shaded regions show $A(S, \Gamma)$ in the range of $\Gamma = 0.4$–1.5 (median value $\Gamma = 1.0$), which represents the interquartile (i.e., 25%–75%) range for the 332 X11 sources with estimates of Γ that were not based on limits. We note that generally $A(S, \Gamma)$ increases with increasing Γ. We find that the $A(S, \Gamma)$ curves asymptote to a value of ≈2 arcmin^2 approaching $S = 0$, suggesting that sources with extremely low fluxes (down to zero) could in principle produce fluctuations exceeding the probability threshold defined in Equation (1). However, as discussed above, such sources would most efficiently be removed using our initial `wavdetect` screening. Therefore, we cannot use information at such flux levels to determine number counts reliably. We therefore choose to restrict our number-count computations to flux levels where >10 arcmin^2 solid angle is accessible in our survey for the case of $\Gamma = 1.4$ (the mean SED of the X-ray background; e.g., Moretti et al. 2009). Our adopted ≈10 arcmin^2 solid-angle limit additionally constrains our flux limits. The resulting limits are 5.1×10^{-18}, 3.7×10^{-17}, 4.6×10^{-17}, and 2.4×10^{-17} erg cm^{-2} s^{-1} for the SB, HB, UHB, and FB, respectively; these are factors of ≈1.9–4.3 times fainter than those of B04 and G08, the previously deepest number-count studies. For the full range of X-ray spectral slopes (i.e., Γ values) in the X11 sample, ≈5–20 arcmin^2 of solid angle is available for number-count computations at the flux limits (above the asymptotic regime). We note that the flux limits derived here are fainter than those presented in X11, which were ≈9.1×10^{-18} and ≈5.5×10^{-17} erg cm^{-2} s^{-1} in the SB and HB, respectively (see also the area curves in our Figure 2 compared with Figure 23 in X11). This is due to the fact that X11 considered only a single count-rate-to-flux conversion factor and did not use the probabilistic approach adopted here.

To account for the fact that, for each X-ray-detected source in our main catalog, we are only able to measure reliably the total observed counts s (see above), the local background b_{ext}, and that the intrinsic flux S may be subject to large uncertainty (particularly in the low-count regime), we consider the conversion from counts to flux for each source to be probabilistic. For each X-ray-detected source, we computed the flux probability distribution as follows:

$$P_{\mathrm{T}} = \frac{(s + b_{\mathrm{ext}})!}{s!\,b_{\mathrm{ext}}!}\left(\frac{T}{T + b_{\mathrm{ext}}}\right)^{s} \times \left(1 - \frac{T}{T + b_{\mathrm{ext}}}\right)^{b_{\mathrm{ext}}} dN/dS\big|_{\mathrm{model}}, \quad (4)$$

where the term $dN/dS\big|_{\mathrm{model}}$ is a Bayesian prior, based on the differential number counts, which accounts for the Eddington bias near the sensitivity limit. As noted in B04, the slope of the number counts of AGNs, normal galaxies, and Galactic stars will differ at the flux limit of the CDF-S. Therefore, $dN/dS\big|_{\mathrm{model}}$ for a given source will depend on which source population it belongs to. Previous studies of X-ray number counts (e.g., Rosati et al. 2002; B04; Kim et al. 2007; G08) have shown that power laws provide good fits to the overall shapes of the log N–log S. To first order, we use priors based on the following power-law parameterizations:

$$\frac{dN}{dS}^{\mathrm{AGN}} = \times \begin{cases} K^{\mathrm{AGN}}(S/S_{\mathrm{ref}})^{-\beta_1^{\mathrm{AGN}}} & (S \leqslant f_{\mathrm{b}}^{\mathrm{AGN}}) \\ K^{\mathrm{AGN}}(f_{\mathrm{b}}/S_{\mathrm{ref}})^{\beta_2^{\mathrm{AGN}}-\beta_1^{\mathrm{AGN}}}(S/S_{\mathrm{ref}})^{-\beta_2^{\mathrm{AGN}}} & (S > f_{\mathrm{b}}^{\mathrm{AGN}}) \end{cases}$$

$$\frac{dN}{dS}^{\mathrm{gal}} = K^{\mathrm{gal}}(S/S_{\mathrm{ref}})^{-\beta^{\mathrm{gal}}}$$

$$\frac{dN}{dS}^{\mathrm{star}} = K^{\mathrm{star}}(S/S_{\mathrm{ref}})^{-\beta^{\mathrm{star}}}, \quad (5)$$

where dN/dS(AGN), dN/dS(gal), and dN/dS(star) are differential number-count parameterizations to be applied to AGNs, normal galaxies, and Galactic stars, respectively, $f_{\mathrm{b}}^{\mathrm{AGN}}$ is the flux related to the break in the double power law used to describe the AGN number counts, and $S_{\mathrm{ref}} \equiv 10^{-14}$ erg cm^{-2} s^{-1}. As we show in Section 3.1 below, we characterize each X-ray source using the X-ray and multiwavelength data and provide best estimates of the parameters in Equation (5) (i.e., K, β, and f_b values) for the AGNs, normal galaxies, and Galactic stars. For each source, we computed P_{T} down to the flux limits defined above and normalize Equation (4) using $\int P_T\ dS = 1$. In Figure 3, we show examples of P_{T} as a function of 0.5–2 keV flux for two AGNs in the main *Chandra* catalog having `AE` probability $P \approx 10^{-45}$ (solid curve) and $P \approx 0.003$ (dashed curve; near the detection threshold). For this computation, we utilized values of $\beta_1^{\mathrm{AGN}} = 1.49$, $\beta_2^{\mathrm{AGN}} = 2.49$, and $f_{\mathrm{b}}^{\mathrm{AGN}} = 5.6 \times 10^{-15}$ erg cm^{-2} s^{-1} (the normalization is arbitrary); as we will show in Section 3.1, these values represent the best-fit parameterizations for AGN SB number counts.

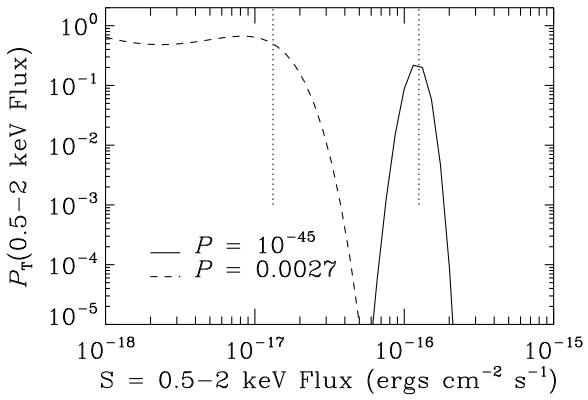

Figure 3. 0.5–2 keV flux probability distributions for two AGNs in the X11 catalog with no-source-detection probabilities (provided by AE) of $\approx 10^{-45}$ (solid curve) and ≈ 0.003 (dashed curve). The latter source is roughly at the boundary of our adopted detection threshold $P_{\rm thresh} = 0.004$ and therefore illustrates the extent to which the flux conversion for sources in the low-count regime with non-negligible Eddington biases can be affected. The vertical dotted lines indicate the most probable single-value flux given in the X11 catalog.

2.2. Cumulative Number-count Computation

Using the above information, we computed cumulative number counts for the ≈4 Ms CDF-S survey using the following integral:

$$N(>S) = \int_S^\infty \left[\sum_{i=1}^{N_{\rm src}} P_{T,i}(S) C_i' / A(S, \Gamma_i) \right] dS, \qquad (6)$$

where the summation is over all X-ray-detected sources in a particular category of sources (e.g., all sources, AGNs, normal galaxies, etc.) and Γ_i represents the effective photon index for source i. For the 332 X-ray sources detected in both the SB and HB, we utilized the photon indices from X11; otherwise, we used $\Gamma = 1.4$. Since $P_{{\rm T},i}$ is dependent on our input Bayesian prior (which depends on source type), the number counts will depend mildly on the choice of our model. The term C' is a count rate and off-axis angle-dependent completeness term, which corrects for the fact that our X-ray point-source catalogs were constructed by (1) running wavdetect to form an initial list of candidate sources and (2) assessing the probability of detection using AE. If we chose to use a catalog based strictly on the AE source-detection probability assessment for every location on the image, then $C' = 1$ for all sources; however, such a catalog would produce large numbers of false sources, leading to significant errors in the number counts at faint fluxes, and is computationally impractical. In practice, the completeness corrections are small perturbations (median $C' \approx 1.00$ for all bands, with ≈95% of sources having $C' \lesssim 1.7$–2.4) and affect number counts near the flux limits. C' and its count rate and off-axis angle dependencies were measured using marx simulations, and a full description of this procedure can be found in the Appendix.

Following the same approach implemented in Section 5 of G08, we utilized maximum-likelihood techniques to optimize the Bayesian model parameters. As discussed above, we made use of power-law differential number-count models for our Bayesian priors (see Equation (5)), which are dependent on source type. For a given source, we first characterized its type (i.e., AGNs, normal galaxy, or Galactic star; see Section 3.1 below), chose an appropriate model in Equation (5), and computed the probability p_i of that source being present in the ≈4 Ms CDF-S catalog as follows:

$$p_i = \frac{\int P_T(S, N_i) dS}{\int dN/dS\big|_{{\rm model},i} A(S, \Gamma_i) dS}, \qquad (7)$$

where N_i represents the total number of counts measured within the extraction cell for each detected source. Considering our model, the total likelihood of obtaining the ≈4 Ms source catalog and its source-count distribution can be computed as $\prod_i p_i$. We maximized the total likelihood for the model input parameters for AGNs, normal galaxies, and Galactic stars separately to find best-fit values for each of the parameters in Equation (5).

3. RESULTS

3.1. Number Counts by Source Type and Total Counts

The extensive multiwavelength data in the ≈4 Ms CDF-S region allow for the robust characterization of the X-ray-detected sources. As described in X11, 716 of the 740 X-ray-detected sources have multiwavelength counterparts, and 673 have either secure spectroscopic or reliable photometric redshifts. Following a similar scheme to that provided by X11, we have classified the X-ray sources in our sample as AGNs, normal star-forming galaxies (hereafter galaxies), and Galactic stars. In this process, we make use of six AGN selection criteria.

1. *X-ray luminosity*. A source with an observed-frame SB, HB, UHB, or FB luminosity (i.e., observed-frame $L_{\rm X} = 4\pi d_L^2 f_{\rm X}$, where d_L is the luminosity distance) $\gtrsim 3 \times 10^{42}$ erg s^{-1} is classified as a luminous AGN. In the nearby universe, the most powerful star-forming galaxies (luminous infrared galaxies) all have $L_{0.5-8\,{\rm keV}} \lesssim 10^{42}$ erg s^{-1} (e.g., Iwasawa et al. 2009, 2011; Lehmer et al. 2010; Pereira-Santaella et al. 2011).
2. *X-ray spectral shape*. A source with an effective photon index of $\Gamma \lesssim 1.0$ is most likely to be dominated by a single powerful X-ray source that is significantly obscured. We consider such sources to be obscured AGNs.
3. *X-ray-to-optical flux ratio*. A source with an X-ray-to-optical flux ratio of $\log(f_{\rm X}/f_R) > 1$ (where $f_{\rm X} = f_{0.5-2\,{\rm keV}}$, $f_{2-8\,{\rm keV}}$, $f_{4-8\,{\rm keV}}$, or $f_{0.5-8\,{\rm keV}}$) is considered to have X-ray emission significantly elevated compared with normal-galaxy processes (e.g., hot gas, low-mass and high-mass X-ray binary emission) as traced by stellar emission (i.e., f_R). Such sources were classified as AGNs.
4. *X-ray-to-radio luminosity ratio*. A source with substantial excess (i.e., a factor of $\gtrsim 5$) X-ray emission over the level expected from pure star formation (i.e., observed-frame SB, HB, FB, or UHB luminosity $\gtrsim 5 \times (8.9 \times 10^{17} L_{1.4\,{\rm GHz}})$; Bauer et al. 2002) is considered to be X-ray overluminous compared with the X-ray/star formation rate (SFR) correlation, and its X-ray emission is therefore likely to be dominated by an AGN. This criterion is similar in nature to that of criterion 3 but differs in that it allows for a more sensitive classification of a subset of actively star-forming galaxies (i.e., detected at 1.4 GHz) using a more reliable tracer of the intrinsic galactic SFR that is insensitive to dust obscuration.
5. *X-ray variability*. Sources found to be variable in the X-ray band (with probability $\gtrsim$95%) on timescales of months to years that also have 0.5–8 keV luminosities greater than 10^{41} erg s^{-1} are unlikely to be produced by normal-galaxy processes (see Young et al. 2012 for details). These sources were classified as AGNs.

6. *Optical spectroscopy*. Finally, sources with optical spectroscopic AGN features such as broad and/or high-excitation emission lines are classified as AGNs. These sources were identified using the spectroscopic catalogs of Szokoly et al. (2004), Mignoli et al. (2005), and Silverman et al. (2010) (see X11 for details).

A source is initially classified as an AGN if at least one of the above six criteria is satisfied. However, we found that five of the sources that were classified as AGNs via the above criteria had 1–2 keV and 0.5–1 keV band ratios that were consistent with being dominated by hot interstellar gas (see Danielson et al. 2012). The initial AGN classification for these five sources was based on having high X-ray-to-optical flux ratios (criterion 3); however, their X-ray luminosities compared with their *B*-band luminosities appear to be consistent with hot-gas-dominated galaxies (see Danielson et al. 2012 for details). We therefore classified these five objects as normal galaxies. In addition to classifying sources directly as AGNs and normal galaxies, we searched for direct multiwavelength indicators of Galactic stars. Likely Galactic stars were identified using (1) optical spectroscopy from Szokoly et al. (2004), Mignoli et al. (2005), and Silverman et al. (2010); (2) *Hubble Space Telescope* (*HST*) stellarity indices >0.7 (from the Caldwell et al. 2008; GEMS catalogs); and (3) best-fit stellar templates from MUSYC photometric redshift fits (Cardamone et al. 2010). All Galactic star candidates were visually screened and obvious normal galaxies were noted. The remaining stellar candidates were then classified as "Galactic stars." Remaining sources that were not classified as either AGNs or stars were classified as normal galaxies. Based on these criteria, we therefore estimate that of the 740 X-ray-detected sources, 561 are AGNs, 169 are normal galaxies, and 10 are Galactic stars.

We compared our normal-galaxy classifications with the 31 radio and X-ray-selected normal galaxies classified by Vattakunnel et al. (2012) and found that 25 sources overlap. We find that four of the Vattakunnel et al. (2012) sources that we classify as AGNs had high X-ray-to-radio luminosity ratios (criterion 4), a criterion that was not implemented by Vattakunnel et al. (2012).

In Figure 4, we plot the observed-frame 0.5–8 keV luminosity versus redshift for the AGNs and normal galaxies with redshift measurements. Our AGN and normal-galaxy samples span redshift ranges of $z \approx 0.1$–8 and $z \approx 0.03$–2.6, respectively. These redshifts are from both photometric and spectroscopic redshift estimates, and all redshift estimates above $z = 4.76$ are based on photometric redshifts. We have chosen to use the most probable photometric redshift for each source; however, some of the $z > 4.76$ sources have photometric redshifts consistent with being at lower redshifts (see Luo et al. 2010 for details).

Using the classifications adopted above and our methods for computing and optimizing number counts described in Section 2, we computed the cumulative number counts for AGNs, normal galaxies, and Galactic stars and determined the best-fit parameters related to their priors (i.e., those characterized in Equation (5)). In Figure 5, we present the breakdown of the cumulative number counts from AGNs, normal galaxies, and Galactic stars for the four bandpasses (discrete symbols). Total number counts for the survey are simply the sum of the number counts from each of these populations. In Figure 6, we show the *differential* number counts (dN/dS) for the four bandpasses. The best-fit dN/dS model parameters, used in computing our number counts, have been tabulated in Table 1, and the cumulative and differential number counts corresponding to these models have been shown in Figures 5 and 6, respectively (continuous curves). In Figure 7, we show sample probability distributions for the best-fit dN/dS model parameters appropriate for AGNs detected in the SB.

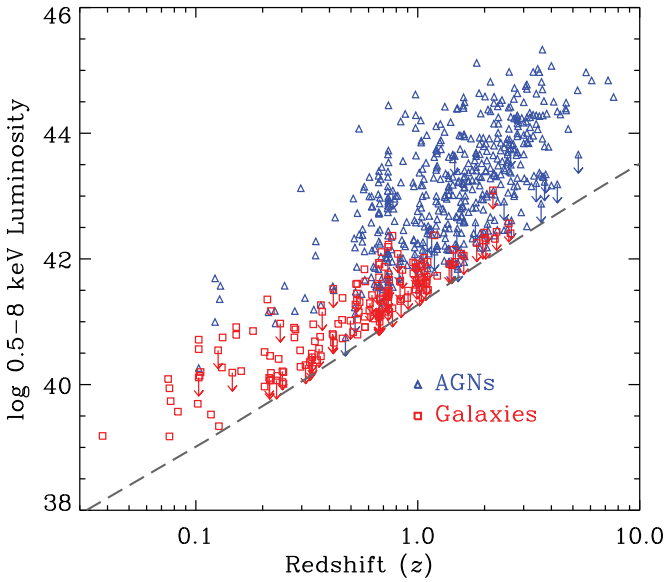

Figure 4. Observed-frame 0.5–8 keV luminosity vs. redshift for AGNs (blue triangles) and normal galaxies (red squares). Luminosities were calculated using the best redshift estimates and 0.5–8 keV fluxes provided by X11 and our adopted cosmology. The dashed curve indicates the observed-frame luminosity corresponding to the flux limit at the center of the ≈4 Ms CDF-S. The normal-galaxy population broadly covers the redshift range $z \approx 0.03$–2.6, and AGNs cover the redshift range of $z \approx 0.1$–8. These redshifts are based on both spectroscopic and photometric redshifts, and all sources at $z > 4.76$ have only photometric redshift estimates. We adopt the most probable photometric redshifts; however, some of the $z > 4.76$ photometric redshifts are consistent with being at lower redshifts (see Luo et al. 2010 for details).

(A color version of this figure is available in the online journal.)

The bottom panels of Figures 5 and 6 show the fractional contribution that the respective cumulative and differential number counts of each source type make to the total counts. We find that AGNs still dominate the cumulative number counts at all flux levels in all four bands; however, at SB and FB fluxes below $\lesssim 10^{-16}$ erg cm^{-2} s^{-1}, normal galaxies undergo a rapid increase in their numbers. At the faintest SB flux limit ($\approx 5.1 \times 10^{-18}$ erg cm^{-2} s^{-1}), AGNs and normal galaxies reach source densities of ≈14,900 and 12,700 deg^{-2}, respectively. These sky densities are factors of ≈2.2 and ≈4.5 times larger than those reported at the ≈2 Ms *Chandra* depth (see B04) for AGNs and normal galaxies, respectively. We find that our SB normal-galaxy number counts lie between the "optimistic" and "pessimistic" estimates from B04 and are in good agreement with previous work by Hornschemeier et al. (2003). Due to the small solid angle of our survey, the bright normal-galaxy number-count data drop off at SB fluxes $\gtrsim 4 \times 10^{-16}$ erg cm^{-2} s^{-1}; however, the extension of our best-fit power-law fit (red dotted curve in Figure 5(a)) agrees well with bright-end normal-galaxy number counts from the *XMM-Newton* serendipitous plus needles in the haystack surveys (Georgakakis et al. 2006) and the *Chandra* Multiwavelength Project (ChaMP; Kim et al. 2006). Normal galaxies constitute 46% ± 5% and 43% ± 5% of the total cumulative number counts in the SB and FB, respectively, a result consistent with that found by X11, who showed that ≈40%–50% of the SB-detected sources within ≈4′ of the ≈4 Ms CDF-S center are normal galaxies

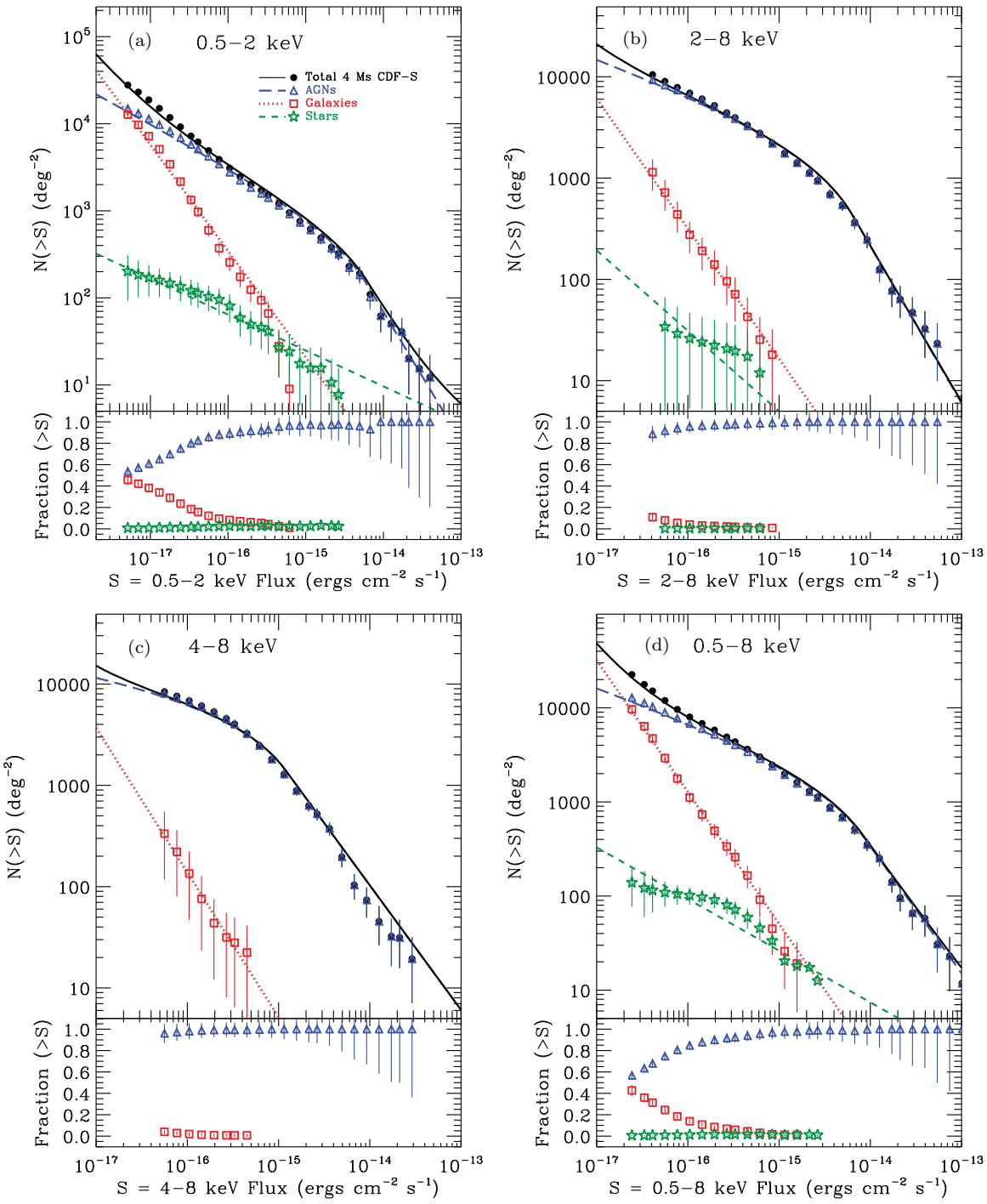

Figure 5. Top panels of (a)–(d): cumulative number counts for the SB (a), HB (b), UHB (c), and FB (d) broken down into AGNs (open blue triangles), normal galaxies (open red squares), and Galactic stars (open green stars). The total number counts have been shown as filled circles. In each plot, the best-fit dN/dS parameterizations based on Equation (5) have been shown as blue long-dashed, red dotted, and green short-dashed curves for AGNs, normal galaxies, and Galactic stars, respectively. The total number-count model, based on summing the three contributing components, has been shown as a black curve. Bottom panels of (a)–(d): fractional contributions from AGNs, normal galaxies, and Galactic stars to the total number counts. For the majority of the flux ranges, AGNs dominate the number counts; however, normal galaxies provide significant contributions near the flux limits of the SB and FB.

(A color version and a machine-readable table of the cumulative number-count data for the ≈4 Ms CDF-S of this figure are available in the online journal.)

(see their Figure 13(c)). This signifies more than a doubling in the fractional contribution that the normal-galaxy cumulative number counts make to the total number counts at the SB flux limit over that found in the ≈2 Ms CDFs (see B04). In terms of the differential number counts, it appears that the contribution from normal galaxies exceeds that of AGNs at SB and FB fluxes below ≈(1–2) $\times 10^{-17}$ erg cm^{-2} s^{-1} and ≈(3–7) $\times 10^{-17}$ erg cm^{-2} s^{-1}, respectively (see Figure 6(a)). We estimate that near the SB and FB flux limits, normal galaxies make up ≈45%–70% of the differential number counts. The rapid increase in normal-galaxy counts signifies that deep *Chandra* surveys are on the verge of being normal-galaxy dominated at the faintest fluxes (see Section 5 for a discussion). In Table 2, we summarize properties of the number counts.

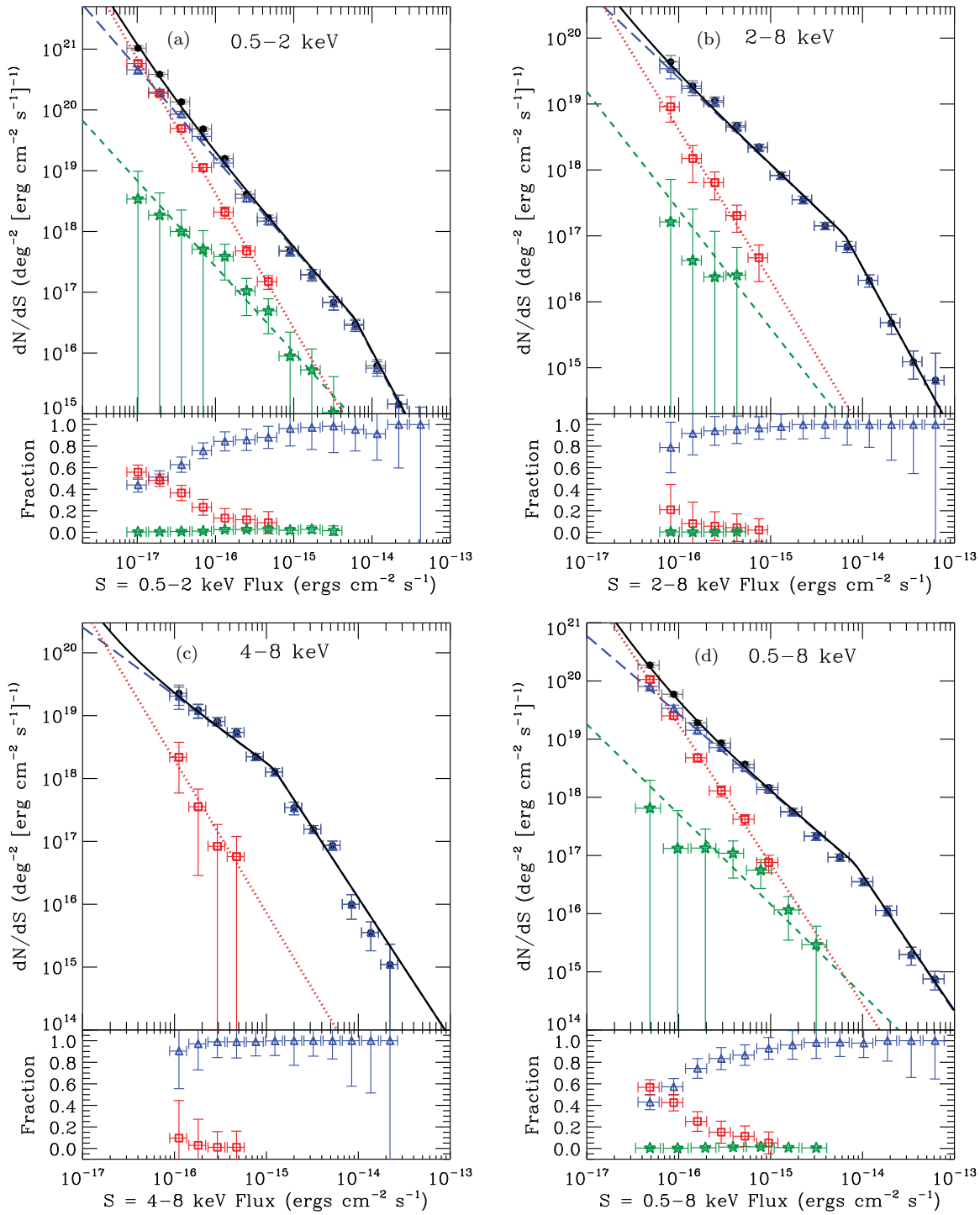

Figure 6. Differential number counts (dN/dS) vs. flux for the SB (a), HB (b), UHB (c), and FB (d), broken down into AGNs (open blue triangles), normal galaxies (open red squares), and Galactic stars (open green stars; for the SB, HB, and FB). The differential number counts have been estimated using flux bins of ≈0.3 dex. In each plot, the best-fit dN/dS parameterizations based on Equation (5) have been shown as blue long-dashed, red dotted, and green short-dashed curves for AGNs, normal galaxies, and Galactic stars, respectively. The total number-count model, based on summing the three contributing components, has been shown as a black curve. Bottom panels of (a)–(d): fractional contributions from AGNs, normal galaxies, and Galactic stars to the differential number counts. In the SB and FB, we find that the differential number counts of normal galaxies appear to surpass those of AGNs for fluxes below ≈(1–2) $\times 10^{-17}$ erg cm^{-2} s^{-1} and ≈(3–7) $\times 10^{-17}$ erg cm^{-2} s^{-1}, respectively.

(A color version of this figure is available in the online journal.)

In Figure 8, we show our derived total number-count distributions normalized by a Euclidean slope of $S^{1.5}$ (i.e., $N(>S) \times (S/S_{\rm ref})^{1.5}$, where $S_{\rm ref} = 10^{-14}$ erg cm^{-2} s^{-1}). The Euclidean representation allows for comparisons with previous investigations at both the faint and bright ends of the distributions. For comparison, we have plotted number-count distributions from previous surveys with *XMM-Newton* (Brunner et al. 2008; Mateos et al. 2008; Cappelluti et al. 2009) and *Chandra* (Bauer et al. 2004; Kim et al. 2007; G08; Luo et al. 2008; Elvis et al. 2009; Puccetti et al. 2009). Some small

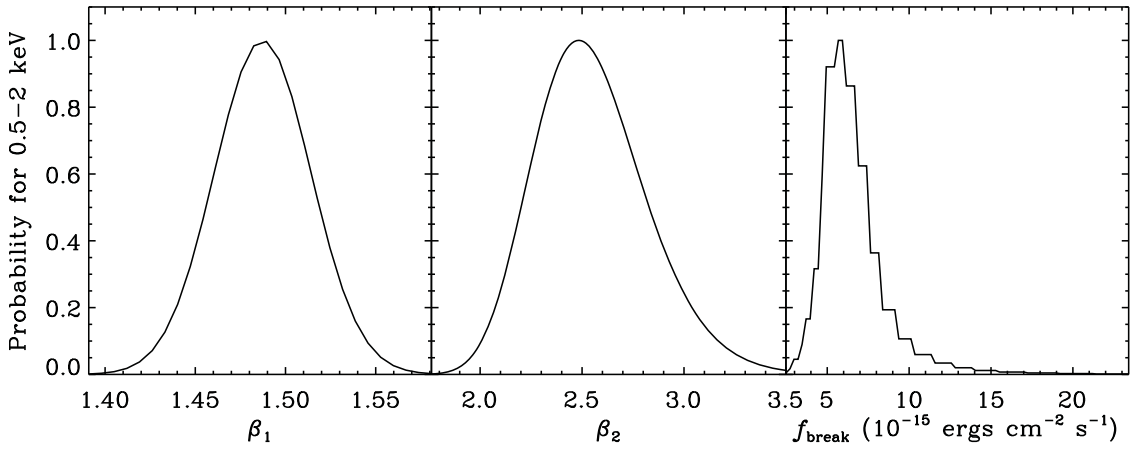

Figure 7. Sample Bayesian dN/dS model parameter ($\beta_1^{\rm AGN}$, $\beta_2^{\rm AGN}$, and $f_{\rm b}^{\rm AGN}$) likelihood distributions (normalized to the maximum likelihood) for the 0.5–2 keV band number counts. These parameters have been summarized in Equation (5), and their values are provided in Table 1.

Table 1
Maximum-likelihood Best-fit Model Parameters

Bandpass	AGNs				Normal Galaxies		Galactic Stars	
	$K_{14}^{\rm AGN}$	$\beta_1^{\rm AGN}$	$\beta_2^{\rm AGN}$	$f_{\rm break}^{\rm AGN}$	$K_{14}^{\rm gal}$	$\beta^{\rm gal}$	$K_{14}^{\rm star}$	$\beta^{\rm star}$
(1)	(2)	(3)	(4)	(5)	(6)	(7)	(8)	(9)
0.5–2 keV	169.56 ± 8.69	1.49 ± 0.03	2.48 ± 0.27	$6.0^{+1.4}_{-1.6}$	1.53 ± 0.10	$2.22^{+0.08}_{-0.07}$	3.97 ± 0.37	$1.41^{+0.14}_{-0.13}$
2–8 keV	573.13 ± 27.49	1.32 ± 0.04	$2.55^{+0.17}_{-0.18}$	6.4 ± 1.0	1.10 ± 0.22	2.29 ± 0.25	0.64 ± 0.22	1.79 ± 0.50
4–8 keV	1463.27 ± 63.61	1.08 ± 0.10	2.23 ± 0.09	$1.2^{+0.7}_{-0.8}$	0.27 ± 0.10	$2.43^{+0.38}_{-0.40}$	...	...
0.5–8 keV	562.20 ± 22.96	$1.34^{+0.04}_{-0.03}$	2.35 ± 0.15	$8.1^{+1.5}_{-1.4}$	2.82 ± 0.26	$2.40^{+0.11}_{-0.12}$	4.07 ± 0.51	$1.55^{+0.19}_{-0.18}$

Notes. Best-fit values and 1σ errors for our number-count priors. Column 1 lists the bandpass. Columns 2–5 provide the double power-law differential number-count parameterization for AGNs, including the normalization $K_{14}^{\rm AGN}$ (Column 2; in units of 10^{14} deg^{-2} (erg cm^{-2} s^{-1})$^{-1}$), faint-end slope $\beta_1^{\rm AGN}$ (Column 3), bright-end slope $\beta_2^{\rm AGN}$ (Column 4), and break-flux $f_{\rm break}^{\rm AGN}$ (Column 5; in units of 10^{-15} erg cm^{-2} s^{-1}). Columns 6 and 7 provide the normal-galaxy single-power-law normalization $K_{14}^{\rm gal}$ and slope $\beta^{\rm gal}$, respectively. Columns 8 and 9 provide the Galactic star single-power-law normalization $K_{14}^{\rm star}$ and slope $\beta^{\rm star}$, respectively. These values were computed using the maximum-likelihood methods described in Section 2.2.

differences in flux measurements (at the $\lesssim$10% level) are expected due to both changes in calibration over the years for *Chandra*[15] and cross-calibration uncertainties between *Chandra* and *XMM-Newton* (see, e.g., Nevalainen et al. 2010). In general, we find good agreement between our number counts and those of previous studies with some minor differences. At faint SB fluxes, we find that our number-count measurements are in good agreement with those of G08 and B04, which are both based on the ≈2 Ms CDF-N and ≈1 Ms CDF-S; however, our estimates are ≈30%–40% lower than those near the limit of the ≈2 Ms CDF-S (L08). It is likely that this discrepancy is due to an incompleteness overcorrection of the faint-end counts in L08. In the HB, we find that our number counts are in good agreement with those of B04 but are somewhat lower than those of G08 and higher than those of L08 (at the ≈10%–20% level in both cases). In the UHB, we find clear evidence of a break in the number counts at $f_{4-8\,\rm keV} \approx 10^{-15}$ erg cm^{-2} s^{-1} (see Figures 5 and 6). Previous investigations of the UHB in the CDF-S revealed no obvious break down to $\approx 7 \times 10^{-16}$ erg cm^{-2} s^{-1} (Rosati et al. 2002), which is very close to where we observe the break. We note that the G08 investigation found a break at a much brighter flux of $\approx 6 \times 10^{-15}$ erg cm^{-2} s^{-1}. In the CDF-S, there are only ≈17 UHB sources brighter than this flux, which would make it difficult to identify such a break if present. In contrast, the G08 analysis made use of wide-area surveys like the EGS, ELAIS-N1, and XBOOTES and therefore have better source statistics at bright UHB fluxes. In all four bands, the ≈4 Ms CDF-S number-count measurements have large uncertainties at bright fluxes due to the relatively small solid angle of the survey; however, we find good general agreement between our measurements and those of previous investigations.

In Sections 3.2 and 3.3 below, we further divide our number-count measurements into contributions from AGN and normal-galaxy subpopulations. For ease of presentation, we discuss only results from the SB and HB; however, full results from all four bandpasses are provided in the tables for reference.

3.2. AGN Number Counts by Redshift, Intrinsic Column Density, and X-Ray Luminosity

As discussed in Section 3.1, AGNs are the majority of the X-ray-detected sources and dominate the cumulative number counts over all fluxes. The ultra-deep *Chandra* data and redshift information allow for first-order estimates of the intrinsic absorption column densities, $N_{\rm H}$, and 0.5–8 keV luminosities, $L_{\rm X}$, of the detected AGNs. Values of $N_{\rm H}$ and $L_{\rm X}$ were estimated following the procedure outlined in Section 3.4 of Xue et al. (2010). The observed X-ray spectrum was modeled using `xspec` (Arnaud 1996) and an assumed absorbed power-law model (`zpow` × `wabs` × `zwabs`). The Galactic column density was

[15] For example, as noted in X11, in 2009 January the *Chandra* ACIS-I ancillary response file (ARF) was updated, resulting in a flat ≈9% reduction in effective area and a ≈0%–8% reduction between 2 and 5 keV (see http://cxc.harvard.edu/ciao/why/caldb4.1.1_hrma.html). Further uncertainties, at the ≈10% level, are expected due to spatial variations of contamination on the optical-blocking filter (see http://web.mit.edu/iachec/meetings/2011/Presentations/Marshall.pdf).

Table 2
Number-counts Statistics

Class	Subclass	Number				Total (deg^{-2})				CXRB Fraction (%)			
		SB	HB	UHB	FB	SB	HB	UHB	FB	SB	HB	UHB	FB
(1)	(2)	(3)	(4)	(5)	(6)	(7)	(8)	(9)	(10)	(11)	(12)	(13)	(14)
All + Bright correction[a]	Total	...	...	...	...	...	...	...	...	75.7 ± 4.3	82.4 ± 13.0	88.4 ± 13.8	81.6 ± 8.9
All	Total	650	403	260	634	27832 ± 1803	10495 ± 871	8387 ± 787	22579 ± 1506	53.1 ± 3.4	66.3 ± 5.8	64.6 ± 6.7	62.7 ± 4.2
AGNs	Total	474	387	256	520	14925 ± 1228	9310 ± 776	8053 ± 757	12802 ± 943	49.0 ± 4.0	65.5 ± 5.8	64.1 ± 6.6	59.6 ± 4.4
	Unknown z	43	21	9	42	2603 ± 545	1058 ± 326	622 ± 249	1906 ± 412	1.1 ± 0.2	1.9 ± 0.6	1.9 ± 0.8	1.8 ± 0.4
	$z = 0.0$–1.5	209	182	123	238	5630 ± 721	3929 ± 478	3677 ± 537	5077 ± 523	31.6 ± 4.0	40.0 ± 5.2	37.9 ± 6.1	37.3 ± 3.8
	$z = 1.5$–3.0	165	133	89	181	5338 ± 763	3111 ± 428	2780 ± 413	4738 ± 612	12.9 ± 1.8	17.7 ± 2.6	17.3 ± 2.8	15.9 ± 2.1
	$z > 3.0$	57	51	35	59	1353 ± 328	1213 ± 289	975 ± 228	1082 ± 266	3.4 ± 0.8	5.9 ± 1.5	7.1 ± 1.8	4.7 ± 1.1
	$\log N_{\rm H} < 22.0$	102	86	51	108	993 ± 105	1559 ± 262	828 ± 159	1572 ± 40	30.3 ± 3.2	21.5 ± 3.9	16.1 ± 3.4	24.7 ± 0.6
	$\log N_{\rm H} = 22.0$–23.0	224	177	115	249	6871 ± 818	4589 ± 558	4157 ± 583	6548 ± 81	14.4 ± 1.7	29.0 ± 3.7	28.1 ± 4.3	24.3 ± 0.3
	$\log N_{\rm H} > 23.0$	105	103	81	121	4458 ± 728	2105 ± 339	2447 ± 382	2777 ± 54	3.1 ± 0.5	13.0 ± 2.2	18.0 ± 3.0	8.9 ± 0.2
	$\log L_{\rm X} < 42.0$	44	23	12	49	2283 ± 544	889 ± 243	803 ± 304	2111 ± 423	1.6 ± 0.4	1.7 ± 0.5	2.0 ± 0.8	1.9 ± 0.4
	$\log L_{\rm X} = 42.0$–43.0	124	86	40	142	5086 ± 704	3247 ± 514	1592 ± 359	5348 ± 677	3.4 ± 0.5	6.3 ± 1.0	6.1 ± 1.5	5.3 ± 0.7
	$\log L_{\rm X} = 43.0$–44.0	167	159	113	186	3818 ± 626	3067 ± 388	3611 ± 485	2534 ± 267	12.4 ± 2.0	21.6 ± 2.9	24.4 ± 3.6	17.9 ± 1.9
	$\log L_{\rm X} > 44.0$	96	98	82	101	1134 ± 167	1050 ± 149	1425 ± 234	904 ± 102	30.4 ± 4.5	34.0 ± 5.2	29.8 ± 5.4	32.7 ± 3.7
Normal galaxies	Total	166	14	4	106	12704 ± 1316	1142 ± 394	334 ± 216	9638 ± 1172	3.0 ± 0.3	0.8 ± 0.3	0.5 ± 0.3	2.6 ± 0.3
	$z \lesssim 0.6$	82	11	3	63	4924 ± 792	975 ± 371	165 ± 155	5049 ± 825	1.6 ± 0.2	0.7 ± 0.2	0.3 ± 0.3	1.6 ± 0.3
	$z \gtrsim 0.6$	84	3	1	43	7770 ± 1052	167 ± 133	...	4573 ± 831	1.4 ± 0.2	0.1 ± 0.1	...	1.0 ± 0.2
	Late-type (star-forming)	123	10	1	74	10174 ± 1191	1051 ± 390	...	7222 ± 1014	2.2 ± 0.3	0.6 ± 0.2	...	1.8 ± 0.3
	Early-type (passive)	43	4	3	32	2530 ± 561	91 ± 53	294 ± 210	2416 ± 588	0.8 ± 0.2	0.2 ± 0.1	0.4 ± 0.3	0.8 ± 0.2
Stars	Total	10	2	...	8	202 ± 109	34 ± 32	...	139 ± 88	1.2 ± 0.6	0.1 ± 0.1	...	0.5 ± 0.3

Notes. Number-count statistics for the source classifications (Column 1) and subclassifications (Column 2) discussed in this paper. Columns 3–6 provide the number of sources in each subclass used in calculating number counts for the four bandpasses. Columns 7–10 provide the number counts for each subcategory at the limiting fluxes for the SB (5.1×10^{-18} erg cm^{-2} s^{-1}), HB (3.7×10^{-17} erg cm^{-2} s^{-1}), UHB (4.6×10^{-17} erg cm^{-2} s^{-1}), and FB (2.4×10^{-17} erg cm^{-2} s^{-1}), respectively. Columns 11–14 provide the integrated intensity (expressed as the percentage of the CXRB intensity) for the SB, HB, UHB, and FB, assuming CXRB intensity values of $(8.15 \pm 0.58) \times 10^{-12}$, $(1.73 \pm 0.23) \times 10^{-11}$, $(1.04 \pm 0.14) \times 10^{-11}$, and $(2.54 \pm 0.24) \times 10^{-11}$ erg cm^{-2} s^{-1} deg^{-2}, respectively (see Section 3.4 for details).

[a] CXRB fractions have been computed using the number-count measurements presented in this paper below 5×10^{-15}, 1.4×10^{-14}, 8.4×10^{-15}, and 2×10^{-15} erg cm^{-2} s^{-1} for the SB, HB, UHB, and FB, respectively, plus bright-end corrections from the Kim et al. (2007) number-count relations (see Section 3.4 for details).

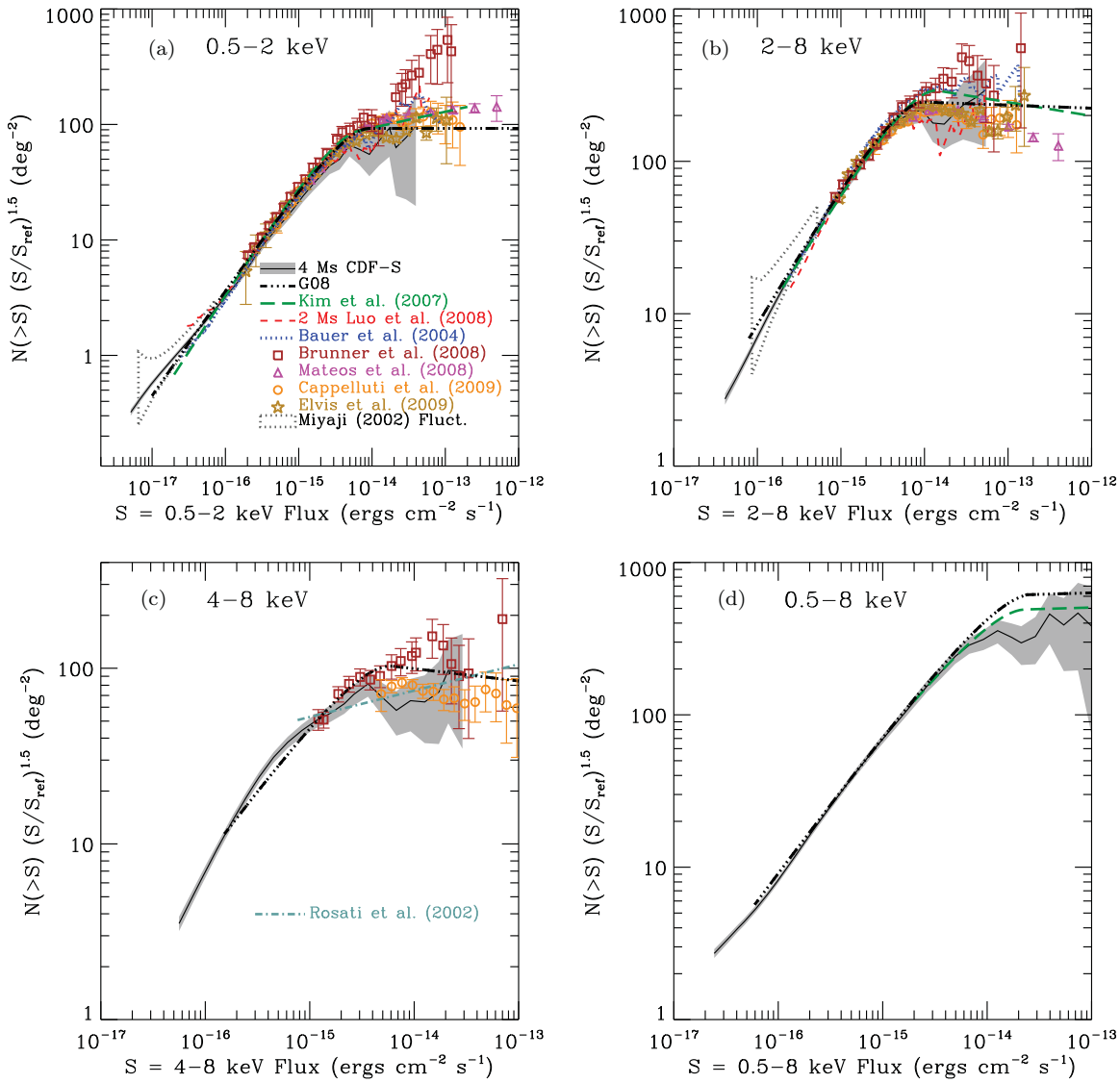

Figure 8. Euclidean-normalized, cumulative number counts ($N(>S) \times (S/S_{\rm ref})^{1.5}$, where $S_{\rm ref} = 10^{-14}$ erg cm^{-2} s^{-1}) and 1σ errors for the ≈4 Ms CDF-S (black curves with gray error bars) for the SB (a), HB (b), UHB (c), and FB (d). The Miyaji & Griffiths (2002) predicted number-count boundaries (from ≈1 Ms fluctuation analyses) are shown as the dotted regions in panels (a) and (b). Previous ≈2 Ms CDF-N plus ≈1 Ms CDF-S number-count estimates from B04 and ≈2 Ms CDF-S number counts from L08 are indicated as blue dotted and red short-dashed curves, respectively. The G08 number counts, which include the ≈2 Ms CDF-N and ≈1 Ms CDF-S surveys, are indicated as dashed triple-dotted curves. Similarly, the ChaMP survey number counts from Kim et al. (2007), which include the ≈2 Ms CDF-N and ≈1 Ms CDF-S surveys, have been shown as green long-dashed curves. Number-count measurements from other *XMM-Newton* and *Chandra* surveys have been indicated, including the *XMM-Newton* serendipitous (Mateos et al. 2008; magenta triangles), Lockman hole (Brunner et al. 2008; brown squares), and COSMOS (Cappelluti et al. 2009; orange circles) surveys, as well as the *Chandra* COSMOS (Elvis et al. 2009; see also Puccetti et al. 2009; gold stars). In the case of the UHB, we highlight the ≈1 Ms CDF-S number counts from Rosati et al. (2002; cyan dot-dashed curve). We note that all measurements shown (i.e., both curves and data points) correspond to measurements, and models are *not* plotted here. We find good overall agreement between our number-count measurements and those found in previous studies.

set to 8.8×10^{19} cm^{-2} (see Section 1), the intrinsic photon index was fixed at $\Gamma_{\rm int} = 1.8$ (e.g., Tozzi et al. 2006), and the best redshift estimate provided in the X11 catalog was adopted. Using this model, we determined the $N_{\rm H}$ value for each AGN that reproduced the observed ratio of count rates between the HB and SB. For sources detected only in the FB an observed spectral index of $\Gamma_{\rm obs} = 1.4$ was adopted. This procedure will be effective for determining $N_{\rm H}$ and $L_{\rm X}$ values for AGNs in the Compton-thin/relatively unobscured regime (i.e., with $N_{\rm H} \lesssim 10^{23}$–$10^{24}$ cm^{-2}) and is less reliable for a minority of sources that are expected to be Compton thick. In the Compton-thick regime, AGN spectra are significantly complex due to the combination of absorption, reflection, scattering, and line emission features that depend on metallicity, ionization state, and geometry (see, e.g., Murphy & Yaqoob 2009). Since most of our sources are in the low-count regime (i.e., $\lesssim$100 counts), such meaningful modeling is beyond our capabilities. Using our power-law model, estimated $N_{\rm H}$, and intrinsic flux $f_{\rm X,int}$ estimates, we computed $L_{\rm X} = 4\pi d_L^2 f_{\rm X,int}(1+z)^{\Gamma_{\rm int}-2}$ for each AGN that had a measured redshift (spectroscopic or photometric).

In Figure 9, we display the breakdown of the AGN number counts in bins of redshift for the SB (left) and HB (right), with the middle panels showing the fractional contribution that sources in each redshift range make to the total AGN number counts. At the brightest fluxes, low-redshift ($z < 1.5$)

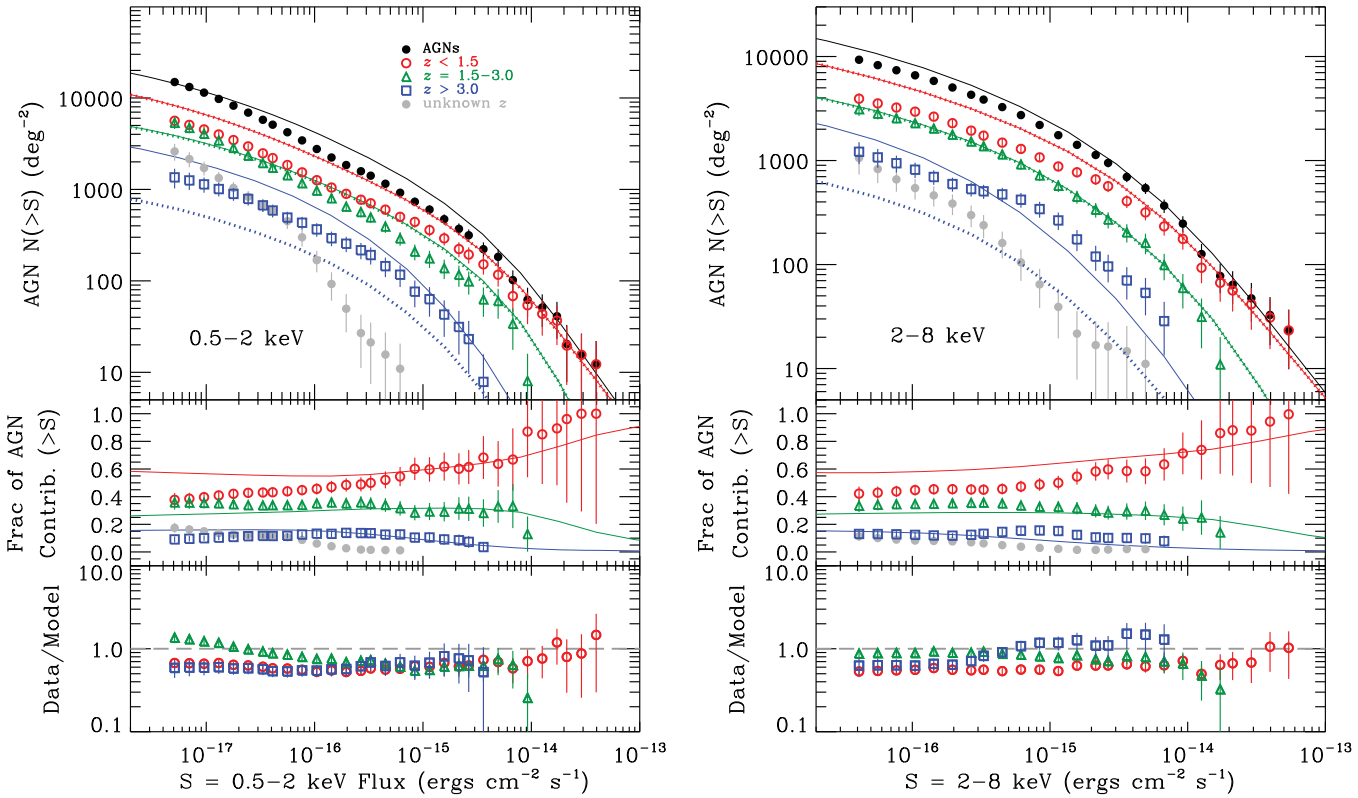

Figure 9. Top panels: cumulative AGN number counts (filled black circles) in the SB (left) and HB (right) broken down by contributions from AGNs in redshift ranges of $z < 1.5$ (open red circles), $z = 1.5$–3 (open green triangles), $z > 3$ (open blue squares), and no measured redshift (filled gray circles). AGN number-count predictions from the AGN population-synthesis models by G07 have been provided both with (dotted curves) and without (solid curves) an exponential decline in the luminosity function at $z > 2.7$. G07 AGN number-count models for all redshifts, $z < 1.5$, $z = 1.5$–3, and $z > 3$ have been shown as black, red, green, and blue curves, respectively. These models are discussed in detail in Section 4.1. Middle panels: fractional contribution that AGNs in each redshift range provide to the overall AGN number counts. The solid curves are the expectations from the G07 model without a declining XLF at $z > 2.7$. Bottom panels: the ratio of the AGN number-count data presented in the top panel divided by the G07 model (without a declining XLF at $z > 2.7$).

(A color version and a machine-readable table of the redshift-divided AGN cumulative number-count data for all four bandpasses of this figure are available in the online journal.)

AGNs dominate; however, going to fainter fluxes, we observe increasing contributions from $z = 1.5$–3 AGNs. At the flux limit of our survey, AGNs at $z = 1.5$–3 make up comparable contributions to the number counts as the $z < 1.5$ AGNs (i.e., ≈40%). For AGNs at $z > 3$, we find a roughly steady fractional contribution to the number counts (≈5%–15%) across the majority of the SB and HB flux ranges where they are detected. In Figure 10, we highlight the SB $z > 3$ AGN number counts and compare them with recent studies from the literature. We find that our number-count measurements for $z > 3$ AGNs are typically a factor of ≈1.5–2 higher than those found in the COSMOS survey fields (i.e., Brusa et al. 2009; Civano et al. 2011) and in good agreement with those from the early ≈4 Ms CDF-S study by Fiore et al. (2012). The difference between our values and those of the COSMOS studies is likely due to differences in $z > 3$ AGN selection techniques, variations in multiwavelength depth and photometric redshift completenesses, and field-to-field variance.

In Figures 11 and 12, we show the breakdown of AGN number counts in bins of intrinsic absorption column density, $N_{\rm H}$, and 0.5–8 keV luminosity, $L_{\rm X}$, for the SB and HB. In both bandpasses, we find that unobscured X-ray-luminous sources dominate the bright-end number counts. Going to fainter fluxes, we find that more obscured and less X-ray-luminous sources make larger contributions. At the SB flux limit, AGNs with $N_{\rm H} \gtrsim 10^{22}$ cm^{-2} and $L_{\rm X} \lesssim 10^{43}$ erg s^{-1} make up the majority of contributions to the number counts. At the HB flux limit, we similarly find that AGNs with $N_{\rm H} \gtrsim 10^{22}$ cm^{-2} dominate the number counts; however, in terms of luminosity, AGNs with $L_{\rm X} \gtrsim 10^{43}$ erg s^{-1} and $\lesssim 10^{43}$ erg s^{-1} make comparable contributions, with the latter population increasing faster.

3.3. Normal-galaxy Counts by Redshift and Morphology

As noted in Section 3.1, normal galaxies compose a significant fraction (≈32%–46%) of the source counts at the SB and FB flux limits. X-ray emission from normal galaxies is expected to be produced by a variety of populations that differ for different galaxy populations (see, e.g., Fabbiano 1989, 2006 for a review). For late-type star-forming galaxies, populations associated with a combination of young and old stellar populations are expected to provide dominant contributions (i.e., high-mass and low-mass X-ray binaries, supernovae and their remnants, hot gas from starburst flows, and young stars; Colbert et al. 2004; Iwasawa et al. 2009, 2011; Lehmer et al. 2010; Pereira-Santaella et al. 2011; Mineo et al. 2012). For passive early-type galaxies, X-ray emission is dominated by low-mass X-ray binaries (LMXBs) and hot X-ray-emitting gas (e.g., O'Sullivan et al. 2001; Gilfanov 2004; Boroson et al. 2011). In this section, we study the normal-galaxy number counts as a function of redshift and morphology.

We measured the number counts of normal galaxies in two redshift bins divided at the median redshift $z_{\rm median} \approx 0.6$. In Figure 13, we show the HB and SB number counts for

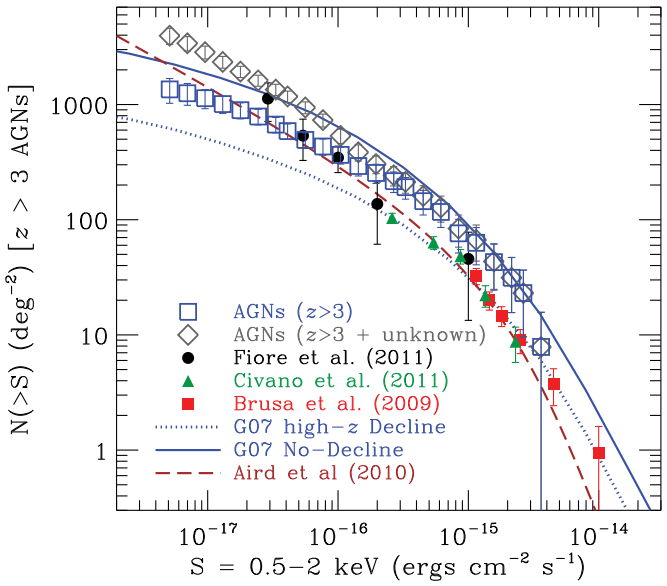

Figure 10. Cumulative SB AGN number counts for sources at redshifts $z \gtrsim 3$. The ≈4 Ms CDF-S estimates and 1σ error bars have been shown as open blue squares with error bars. If we add to the $z \gtrsim 3$ AGN number counts the number counts for X-ray-detected sources without known redshifts, we obtain the open gray diamonds with error bars. Due to their lack of multiwavelength counterparts, in regions where extensive multiwavelength coverage is available, the sources with unknown redshifts are good candidates for being at $z \gtrsim 3$. Recent constraints from Fiore et al. (2012) for the ≈4 Ms CDF-S (filled black circles), Civano et al. (2011) for *Chandra* COSMOS (filled green triangles), and Brusa et al. (2009) for *XMM-Newton* COSMOS (filled red squares) have been shown for comparison. The G07 models for $z \gtrsim 3$ number counts have been shown for the cases where a high-redshift ($z > 2.7$) space-density decline is included (blue dotted curve) and is not (blue solid curve) included. The recent number-count predictions, based on the Aird et al. (2010) XLF measurement in the 2–10 keV band, are shown as a brown long-dashed curve.

(A color version of this figure is available in the online journal.)

normal galaxies at $z \lesssim 0.6$ and $z \gtrsim 0.6$. In the SB, we find that low-redshift ($z \lesssim 0.6$) normal galaxies dominate the bright-end counts; however, below flux levels of ≈(1–2) $\times 10^{-17}$ erg cm^{-2} s^{-1}, high-redshift ($z \gtrsim 0.6$) normal galaxies become the dominant galaxy population. By contrast, normal-galaxy number counts in the HB are dominated by low-redshift normal galaxies across the full flux range, with ≲20% of the number counts being from the high-redshift population.

To characterize the number counts of normal galaxies divided by morphology, we made use of the multiwavelength data to classify the normal galaxies broadly as either late-type or early-type galaxies. We matched the 169 X-ray-detected normal galaxies to the optical source catalogs constructed by Xue et al. (2010), which provide rest-frame optical magnitudes based on SED fitting. To distinguish between relatively blue late-type galaxies and red early-type galaxies, we made use of the rest-frame $U-V$ color. As described by Bell et al. (2004), the U and V bandpass pair straddle the 4000 Å break and as a color provide a first-order indicator of the stellar age of the galactic stellar population. We applied the empirically calibrated redshift-dependent color division calculated in Section 5 of Bell et al. (2004) to separate active blue and passive red galaxy populations. This division was set at

$$(U-V)_{\rm rest} = 1.15 - 0.31z - 0.08(M_V + 20.7), \quad (8)$$

such that galaxies redward and blueward of this division are candidate early-type and late-type galaxies, respectively. We note that a single color division will not perfectly isolate the early-type and late-type galaxy populations. For example, edge-on or dusty late-type galaxies may be artificially reddened and therefore classified as being early-type galaxies (see, e.g., Cardamone et al. 2010; Lusso et al. 2011). Furthermore, intrinsic scatter in the optical color distributions near the color cut will sometimes displace galaxies to the wrong side of the color division (e.g., "green" early-type galaxies that undergo low levels of recent star formation). We therefore visually inspected *HST* z_{850}-band images of all 169 galaxies to identify obvious cases where rest-frame colors provided incorrect morphological classifications. We found that 25 galaxies (≈15%) had obviously incorrect initial morphological classifications that were corrected.

Out of the 169 normal galaxies, we classified 123 as late-type and 43 as early-type galaxies. In Figure 14, we show example *HST* three-color (B_{435}, V_{606}, and z_{850}) images of 10 early-type (top) and 10 late-type (bottom) galaxies that were in the normal-galaxy sample. Following the prescriptions discussed in Section 2, we computed number counts for each of these populations. In Figure 15, we show the number counts of the normal galaxies broken down by optical morphology. The normal-galaxy number counts for early-type and late-type galaxies are comparable at the brightest SB and HB flux levels. Progressing to lower fluxes, however, we find that the late-type galaxy population quickly rises and dominates the normal-galaxy number counts, and at the survey flux limits, late-type galaxies compose ≈80% and ≈90% of the normal-galaxy number counts for the SB and HB, respectively (see lower panels of Figure 15).

3.4. Contributions to the Cosmic X-Ray Background

With the number-count estimates derived above, we can measure the corresponding contributions each source type and subtype make to the extragalactic CXRB. Hereafter, we adopt CXRB intensities $\Omega_{\rm CXRB}$ of $(8.15 \pm 0.58) \times 10^{-12}$ erg cm^{-2} s^{-1} deg^{-2} and $(1.73 \pm 0.23) \times 10^{-11}$ erg cm^{-2} s^{-1} deg^{-2} for the SB and HB, respectively. These CXRB intensities were computed by summing components from (1) the ≈1 Ms CDF-S unresolved background intensity ($\Omega_{\rm unres}$; Hickox & Markevitch 2006), (2) the intensity of faint ≈1 Ms CDF-S sources ($\Omega_{\rm faint}$; below $\approx 5 \times 10^{-15}$ erg cm^{-2} s^{-1} and $\approx 1.4 \times 10^{-14}$ erg cm^{-2} s^{-1} for the SB and HB, respectively) as derived by Hickox & Markevitch (2006; see their Table 5), and (3) the bright-source intensity ($\Omega_{\rm bright}$) derived from the best-fit number-count relations by Kim et al. (2007), which are based on ∼5500 X-ray sources from the ChaMP (e.g., Green et al. 2004; Kim et al. 2004a, 2004b). In the bright-source case, $\Omega_{\rm bright} = \int_{S_{\rm faint}}^{S_{\rm bright}} S'(dN/dS')dS'$, where $S_{\rm faint}$ is the brightest flux used to compute the faint-end counts, $S_{\rm bright} = 10^{-11}$ erg cm^{-2} s^{-1} (for both the SB and HB), and dN/dS' is the best-fit differential number-count model from Table 3 of Kim et al. (2007). Thus, we derived $\Omega_{\rm CXRB} = \Omega_{\rm unres} + \Omega_{\rm faint} + \Omega_{\rm bright}$ for the SB and HB. For the FB and UHB, we adopted values of $(2.54 \pm 0.24) \times 10^{-11}$ erg cm^{-2} s^{-1} deg^{-2} (the sum of the SB and HB CXRB intensities) and $(1.04 \pm 0.23) \times 10^{-11}$ erg cm^{-2} s^{-1} deg^{-2}, respectively. The UHB CXRB intensity was computed by converting the HB intensity to UHB assuming a power-law SED with $\Gamma = 1.4$ (see Moretti et al. 2009).

In Table 2 (Columns 11–14), we provide the intensities and fractional CXRB contributions that sources in various subcategories in the ≈4 Ms CDF-S provide. We find that the vast majority of the CXRB in each band is expected to be produced by AGNs, with normal galaxies producing only a small fraction

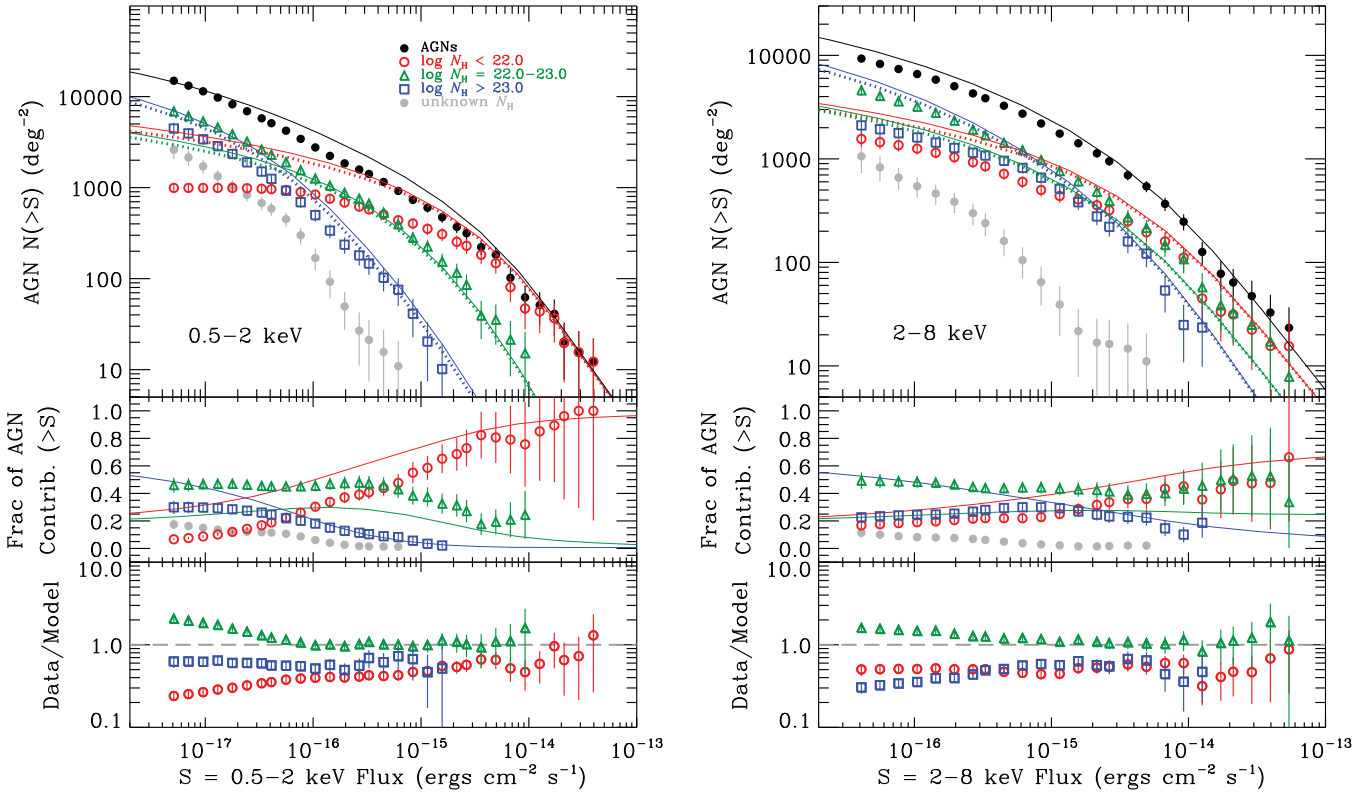

Figure 11. Same as Figure 9, but for AGNs divided into ranges of intrinsic column density ($\log(N_H/cm^{-2}) < 22$ (open red circles), $\log(N_H/cm^{-2}) = 22$–23 (open green triangles), $\log(N_H/cm^{-2}) > 23$ (open blue squares), and no measured N_H due to lack of redshift measurements (filled gray circles)). As in Figure 9, AGN number-count predictions from G07 have been provided as dotted and solid curves, corresponding respectively to the inclusion and exclusion of an exponential decline in the AGN space density at $z > 2.7$ (model curve colors correspond to symbol colors).

(A color version and a machine-readable table of the N_H-divided AGN cumulative number-count data for all four bandpasses of this figure are available in the online journal.)

(≈0.5%–3.0%) of the intensities. These results are similar to those found by B04, although revised to fainter flux levels.

Due to the relatively small solid-angle coverage of the CDF-S survey (≈465 arcmin^2), we are unable to characterize the number counts for the relatively rare X-ray bright-source population (i.e., $S \gtrsim (1\text{–}10) \times 10^{-14}$ erg cm^{-2} s^{-1}). To characterize the bright-end counts for each source type and subtype listed in Table 2 (Column 2) would require a wider survey with equivalent multiwavelength data to that used here for the ≈4 Ms CDF-S. Despite this limitation, we can utilize our number-count estimates and the total bright-end CXRB intensities (i.e., Ω_{bright}) to estimate the total resolved CXRB intensities. In the first row of Table 2, we provide the bright-end-corrected resolved source intensities and fractional contributions to the CXRB. We find that ≈76%–88% of the CXRB intensity can be attributed to X-ray point sources, with the resolved fraction appearing to increase with median bandpass energy; however, a constant or decreasing resolved fraction with energy is not formally ruled out. Comparisons with past studies indicate a variety of levels of consistency with this result. For example, the studies of Hickox & Markevitch (2006) and Kim et al. (2007), which were used to estimate the total CXRB intensities and bright-end corrections for the CDF-S, find similar resolved CXRB fractions (using ≈1–2 Ms depth CDF data) over the same energy ranges studied here. However, the studies of Moretti et al. (2003), B04, Worsley et al. (2005), and G08 find that the resolved CXRB fraction appears to decline somewhat with energy, using data that reach similar *Chandra* depths (≈1–2 Ms). These studies adopt results from either Moretti et al. (2003) and/or De Luca & Molendi (2004) when estimating the CXRB intensity and bright-end counts. We note, however, that even in these studies, the apparent decline in resolved CXRB with energy is less significant in the CDF-S itself (see, e.g., Figure 2 of Worsley et al. 2005). We estimate that between the ≈1–2 Ms and ≈4 Ms depths, the fraction of the resolved CXRB has increased by only ≈1%–2%, which is much smaller than the error bars of our measurements. Therefore, differences between previous resolved CXRB fractions are primarily related to either differing assumptions about the CXRB intensity and bright-end counts or field-to-field variations. In support of the latter point, L08 find that the CDF-S number counts are lower than those of the CDF-N by ≈25% at the faintest fluxes.

4. COMPARISONS WITH MODELS

4.1. The AGN Number Counts and the Evolution of Accreting SMBHs

The redshift-dependent AGN number counts (Figures 9 and 10) provide a directly observable signature of the evolution of AGN activity in the universe. Since AGNs are the brightest X-ray-detected population, many previous investigations have focused on measuring their cosmic evolution (see Brandt & Hasinger 2005 for a review) and, in particular, the evolution of their X-ray luminosity function (XLF; e.g., Cowie et al. 2003; Ueda et al. 2003; Hasinger et al. 2005; Silverman et al. 2008; Ebrero et al. 2009; Aird et al. 2010). For example, Hasinger et al. (2005) made use of a variety of *ROSAT*, *XMM-Newton*, and *Chandra* surveys with highly complete optical/near-IR

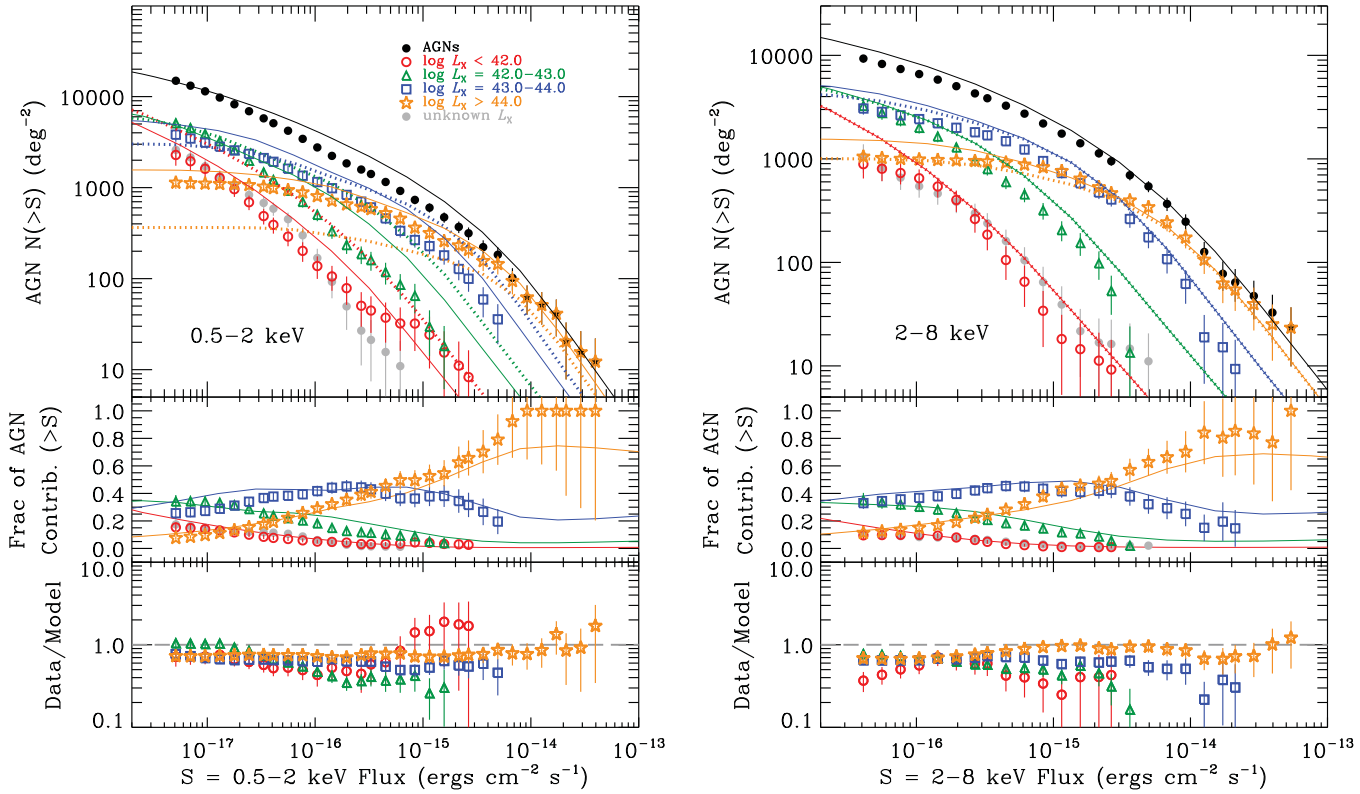

Figure 12. Same as Figure 9, but for AGNs divided into ranges of intrinsic 0.5–8 keV luminosity ($\log(L_X/\mathrm{erg\,s^{-1}}) < 42$ (open red circles), $\log(L_X/\mathrm{erg\,s^{-1}}) =$ 42–43 (open green triangles), $\log(L_X/\mathrm{erg\,s^{-1}}) = 43$–44 (open blue squares), $\log(L_X/\mathrm{erg\,s^{-1}}) > 44$ (open orange stars), and no measured L_X due to lack of redshift measurements (filled gray circles)). As in Figure 9, AGN number-count predictions from G07 have been provided as dotted and solid curves, corresponding respectively to the inclusion and exclusion of an exponential decline in the AGN space density at $z > 2.7$ (model curve colors correspond to symbol colors).

(A color version and a machine-readable table of the L_X-divided AGN cumulative number-count data for all four bandpasses of this figure are available in the online journal.)

redshift measurements to compute the observed evolution of the AGN XLF. This investigation found that X-ray-selected AGNs appear to undergo luminosity-dependent density evolution in their populations, where the space density of low-luminosity (Seyfert-type) AGNs peaks at $z \lesssim 1$ and the highly luminous (QSO-type) AGN space density peaks at $z \approx 2$. These direct measurements of the observed XLF evolution of AGN activity in the universe provide a useful constraint on the SMBH accretion history; however, the observed X-ray bandpass used to make these measurements (i.e., ≈0.5–2 keV) is susceptible to extinction, and therefore populations of AGNs with intrinsic X-ray absorption columns of $N_H \gtrsim 10^{22}$ cm^{-2} will have underrepresented intrinsic accretion activity.

Using the unresolved hard X-ray (≈3–100 keV) background intensity spectrum as a constraint on the obscured ($N_H \approx 10^{22}$–10^{24} cm^{-2}) and Compton-thick ($N_H \gtrsim 10^{24}$ cm^{-2}) AGN populations, Gilli et al. (2007; hereafter G07) used the observed XLF evolution from Hasinger et al. (2005), local distributions of the luminosity-dependent obscured-to-unobscured AGN fraction, and a model distribution of AGN population column densities to form phenomenological models describing the intrinsic evolution of the AGN XLF (see also Ueda et al. 2003; Draper & Ballantyne 2009; Treister et al. 2009 for additional prescriptions). These models make direct predictions for the number-count distributions of sources with different ranges of z, N_H, and intrinsic 0.5–8 keV luminosity L_X[16] and can be directly compared with our observed AGN number-count subpopulations (see Figures 9–12).

In Figures 9–12, we have highlighted the number-count predictions for z, N_H, and L_X selected AGNs by G07 appropriate for the Hasinger et al. (2005) XLF as observed (solid curves) and after applying a high-redshift ($z > 2.7$) exponential decline to the XLF (dotted curves; see Schmidt et al. 1995 for motivation). In general, we found better agreement by not including the exponential declining term (i.e., the solid curves in Figures 9–12). However, since the majority of the AGNs in this study are at $z \lesssim 2.7$, there is generally little difference between the models that include and do not include an exponentially declining term. For clarity in comparisons, in Figures 9, 11, and 12 we have provided lower panels showing the ratio between our observed number counts and the G07 models without the exponential declining term.

For redshift-selected number counts, we found reasonable agreement (within a factor of ≈2) between the observed number counts and the G07 model across the entire SB and HB flux ranges (see Figure 9). We note that a non-negligible fraction of the AGN population does not have redshifts available. Since the multiwavelength coverage over the entire CDF-S is extensive and deep, sources without redshifts (neither spectroscopic nor photometric) have very faint optical/near-IR counterparts and are therefore good candidates for high-redshift ($z > 3$) AGNs. If we add the number counts from AGNs without redshifts to the $z > 3$ number counts, we find improved agreement with the G07 model prediction (see Figure 10, diamonds). For comparison, we have also plotted the predictions from the recent work by Aird

[16] The G07 phenomenological model number-count predictions can be found at http://www.bo.astro.it/~gilli/counts.html.

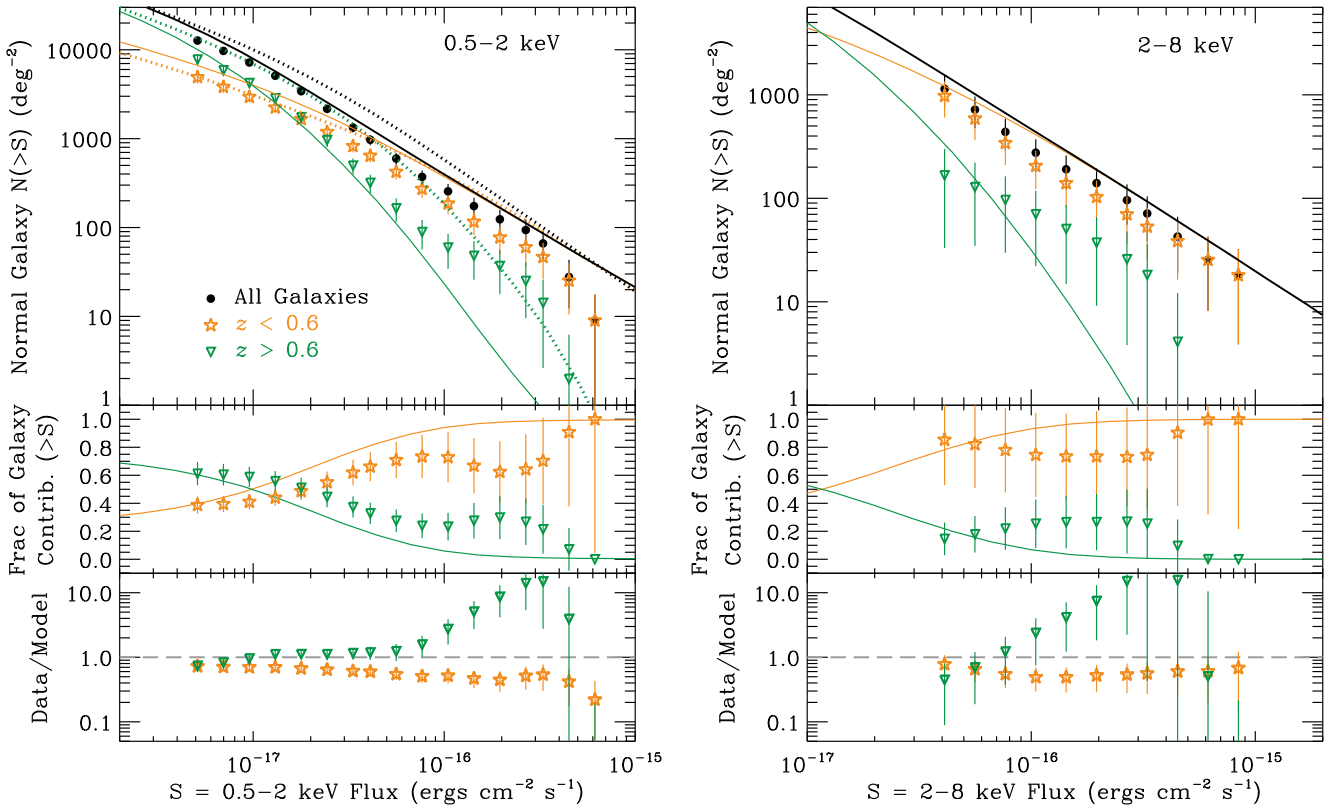

Figure 13. Top panels: cumulative normal-galaxy number counts (filled black circles) in the SB (left) and HB (right) broken down by contributions from galaxies at redshifts $z \lesssim 0.6$ (open orange stars) and $z \gtrsim 0.6$ (open green upside-down triangles). The redshift division between the two normal-galaxy samples was made at the median galaxy redshift. The dotted curves in the left panel show the predicted $z \lesssim 0.6$ (orange dotted curve) and $z \gtrsim 0.6$ (green dotted curve) number counts based on the observed XLF pure-luminosity evolution parameterization derived by Ptak et al. (2007) using observed XLFs out to $z \approx 0.75$. At $z \gtrsim 0.6$, these predictions are based on an extrapolation of the XLF parameterization out to $z \approx 2$. The solid curves in the left and right panels show the predicted number counts for $z \lesssim 0.6$ (orange solid curves) and $z \gtrsim 0.6$ (green solid curves) galaxy populations based on the observed evolution of stellar-mass functions converted to XLFs using X-ray scaling relations (see Section 4.2 for details). Middle panels: the fractional contributions that $z \lesssim 0.6$ and $z \gtrsim 0.6$ galaxy populations make to the total galaxy number counts. Bottom panels: the ratio between the data and predictions based on the solid curves in the top panels.

(A color version and a machine-readable table of the redshift-divided normal-galaxy cumulative number-count data for all four bandpasses of this figure are available in the online journal.)

et al. (2010), which is based on 2–10 keV XLF measurements from the CDFs and the AEGIS-X surveys. The Aird et al. (2010) predictions are also consistent with our $z > 3$ AGN number counts; however, if all of the AGNs with unknown redshifts are in the $z > 3$ range, our number counts become more consistent with the G07 model. Regardless of the redshifts of the sources lacking redshift identifications, our number counts appear to be a factor of $\gtrsim$2 higher than those predicted by the G07 model with exponential decline.

For the number-count predictions based on $N_{\rm H}$, we find significant discrepancies (factors of $\approx$1.5–3) between those observed and those predicted by the G07 model (see bottom panels of Figure 11). This situation is similar regardless of whether the exponential decline is applied or not. We suspect that some of the disagreement here will be due to (1) cosmic variance of the populations, (2) our simplistic calculation of $N_{\rm H}$ based on band ratios (see discussion in Section 3.2), which differs from the spectral models from G07 (see their Figure 1), (3) the distribution of $N_{\rm H}$ values for sources without redshifts, and (4) imperfections in the G07 model descriptions. Regarding point (3), we note that sources with unknown redshifts have a median effective photon index of $\Gamma_{\rm median} \approx 0.7$, which is somewhat harder (softer) than the $\Gamma_{\rm median} \approx 1.0$ ($\Gamma_{\rm median} \approx 0.4$) for sources with $\log(N_{\rm H}/{\rm cm}^{-2}) = 22$–$23$ ($\log(N_{\rm H}/{\rm cm}^{-2}) > 23$). Therefore, we expect that most of the sources with unknown redshifts will have $\log(N_{\rm H}/{\rm cm}^{-2}) \gtrsim 23$ regardless of their redshifts. This would improve the agreement between observed and model number counts for $\log(N_{\rm H}/{\rm cm}^{-2}) \gtrsim 23$. Despite the apparent disagreements and limitations, we do find basic agreement in the general trend: more heavily obscured AGNs have larger contributions at fainter fluxes.

For number counts divided by intrinsic 0.5–8 keV luminosity $L_{\rm X}$, we find good (within a factor of $\approx$2) basic agreement between our measurements and the G07 model (see Figure 12); however, this is not true for the decline model (see dotted curves in upper panels of Figure 12).

In summary, we find that the G07 phenomenological models provide a good description of the redshift, column density, and intrinsic luminosity distributions to the extent that we can constrain these values observationally. Better measurements of the column densities and $L_{\rm X}$ would be needed to improve these models further. However, unless a significant fraction of objects with photometric redshifts $z > 3$ prove to be lower-redshift contaminants, we do find that applying an exponential decline to the AGN XLFs at $z > 2.7$, under the G07 parameterizations, provides a poor characterization of the redshift- and $L_{\rm X}$-divided number counts.

4.2. The Rapidly Increasing Normal-galaxy Counts

In Section 3.3, we presented number-count estimates for the normal-galaxy population and subpopulations separated by

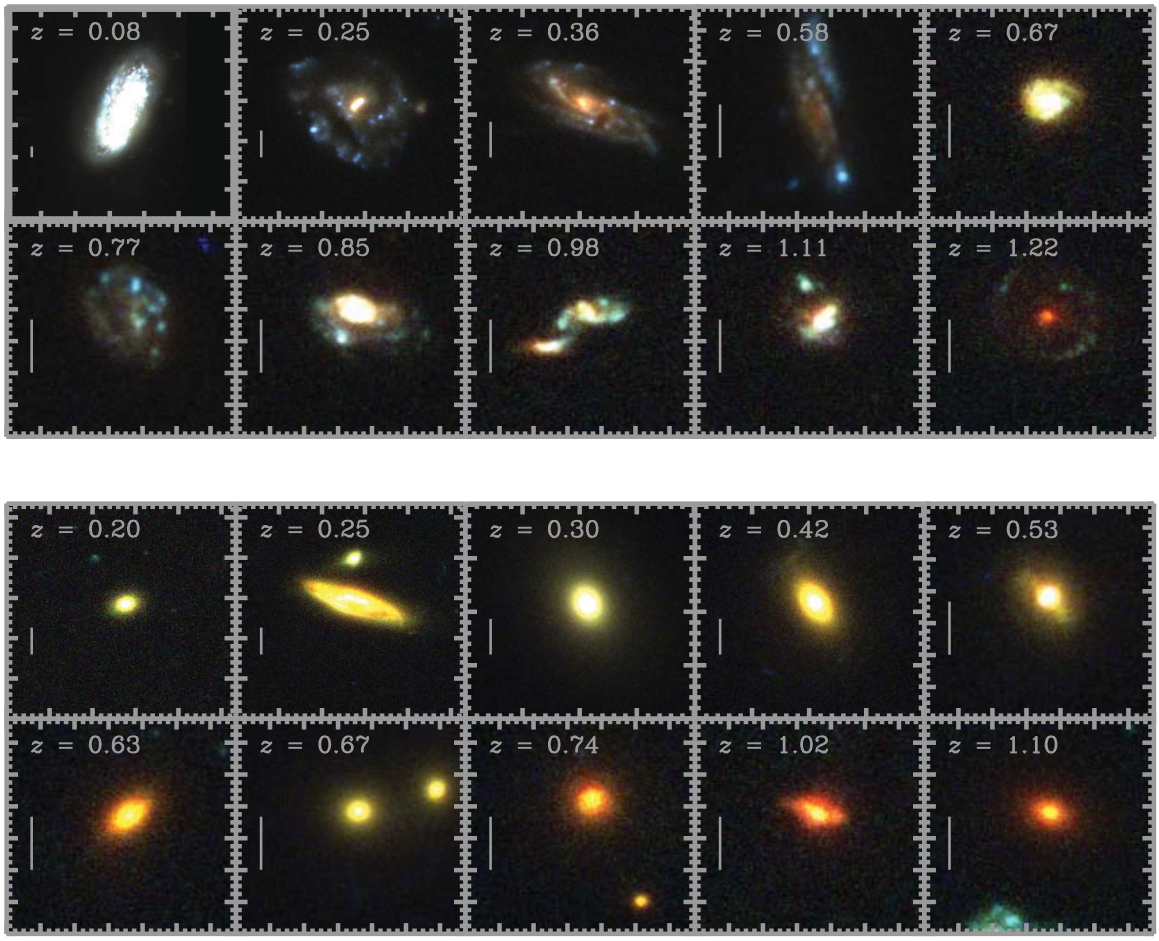

Figure 14. Three-color (B_{435}, V_{606}, and z_{850}) *HST* images of a sample of X-ray-detected normal galaxies ordered by redshift. The top panels show 10 example late-type galaxies, and the bottom panels show 10 example early-type galaxies. The angular extent of each image has been chosen to subtend a physical distance of ≈30 kpc on a side in the rest frame of each galaxy. The redshift of each source is indicated in the upper left, and a 1 arcsec bar has been placed in the lower-left hand corner to show angular scale. The images are centered on the coordinates corresponding to each galaxy, which were taken from Columns 18 and 19 of Table 3 in X11. These positions were obtained primarily from VLT WFI observations, and therefore small ($\lesssim$0.1–0.2 arcsec) offsets are sometimes seen in these *HST* images (note the angular scale).

redshift and galaxy morphology. Given that these X-ray source populations are uniquely accessible to the ultra-deep survey regime probed by the *Chandra* Deep Fields, the evolution of the normal-galaxy XLFs has not been as well characterized as those of AGN populations (see Section 4.1). However, initial investigations have placed first-order constraints on the evolution of normal-galaxy XLFs out to $z \approx 0.75$ (e.g., Norman et al. 2004; Georgakakis et al. 2007; Ptak et al. 2007; Tzanavaris & Georgantopoulos 2008). These investigations have provided evidence for a rapidly increasing late-type galaxy 0.5–2 keV XLF that is consistent with pure-luminosity evolution, where $L^* \propto (1+z)^b$, and $b \approx 1.5$–3. By contrast, the early-type galaxy 0.5–2 keV XLF appears to be changing more slowly with redshift, and in the Tzanavaris & Georgantopoulos (2008) study, the XLF is consistent with being constant or decreasing with redshift (the value of b ranges from ≈ -2.3 to $+2.6$ in these studies). However, these results are based on shallower data than the ≈4 Ms CDF-S and thus far provide only estimates for how the bright end of the galaxy XLFs evolved out to $z \approx 0.75$. In the ≈4 Ms CDF-S, ≈29% of the normal galaxies are at $z \gtrsim 0.75$, and the majority of these sources are only accessible by this survey. In the paragraphs below, we interpret the number counts of the normal-galaxy subpopulations (e.g., see Figures 13 and 15) in the context of what we expect from previous estimates of the galaxy XLF evolution and the evolution of galaxy properties (e.g., SFR and stellar mass) and X-ray scaling relations (e.g., the X-ray/SFR relation).

Following the formalism of Ranalli et al. (2005), the normal-galaxy number counts can be expressed as the following double integral:

$$N(>S) = K_{\rm sr}^{\rm deg} \int_{z_{\rm min}}^{z_{\rm max}} dz \int_{L_{\rm min}(S)}^{L_{\rm max}} \varphi_{\rm X}(\log L_{\rm X}, z)\, d\log L_{\rm X} \frac{dV}{dz d\Omega}, \quad (9)$$

where $K_{\rm sr}^{\rm deg} = 3.05 \times 10^{-4}$ converts from sr^{-1} to deg^{-2}, $\varphi_{\rm X}$ is the redshift-dependent XLF, $dV/dzd\Omega$ is the cosmology-dependent differential volume element (comoving volume per unit redshift per unit solid angle), and $[z_{\rm min}, z_{\rm max}]$ and $[L_{\rm min}(S), L_{\rm max}]$ are, respectively, redshift and luminosity integration limits. The value of $L_{\rm min}(S)$ is the rest-frame luminosity corresponding to a flux S and redshift z. In the upper-left panels of Figures 13 and 15, the dotted curves show 0.5–2 keV number-count predictions based on previous measurements of the evolution of galaxy XLFs for redshift- and morphology-divided galaxy populations, respectively. These curves were computed using the Ptak et al. (2007) redshift-dependent Schechter parameterizations of the observed galaxy XLFs, which assume pure-luminosity evolution of the form $L^* \propto (1+z)^{2.3}$ and $(1+z)^{1.6}$ for late-types and early-types, respectively. We also experimented with using a log-normal parameterization of the galaxy XLF and found

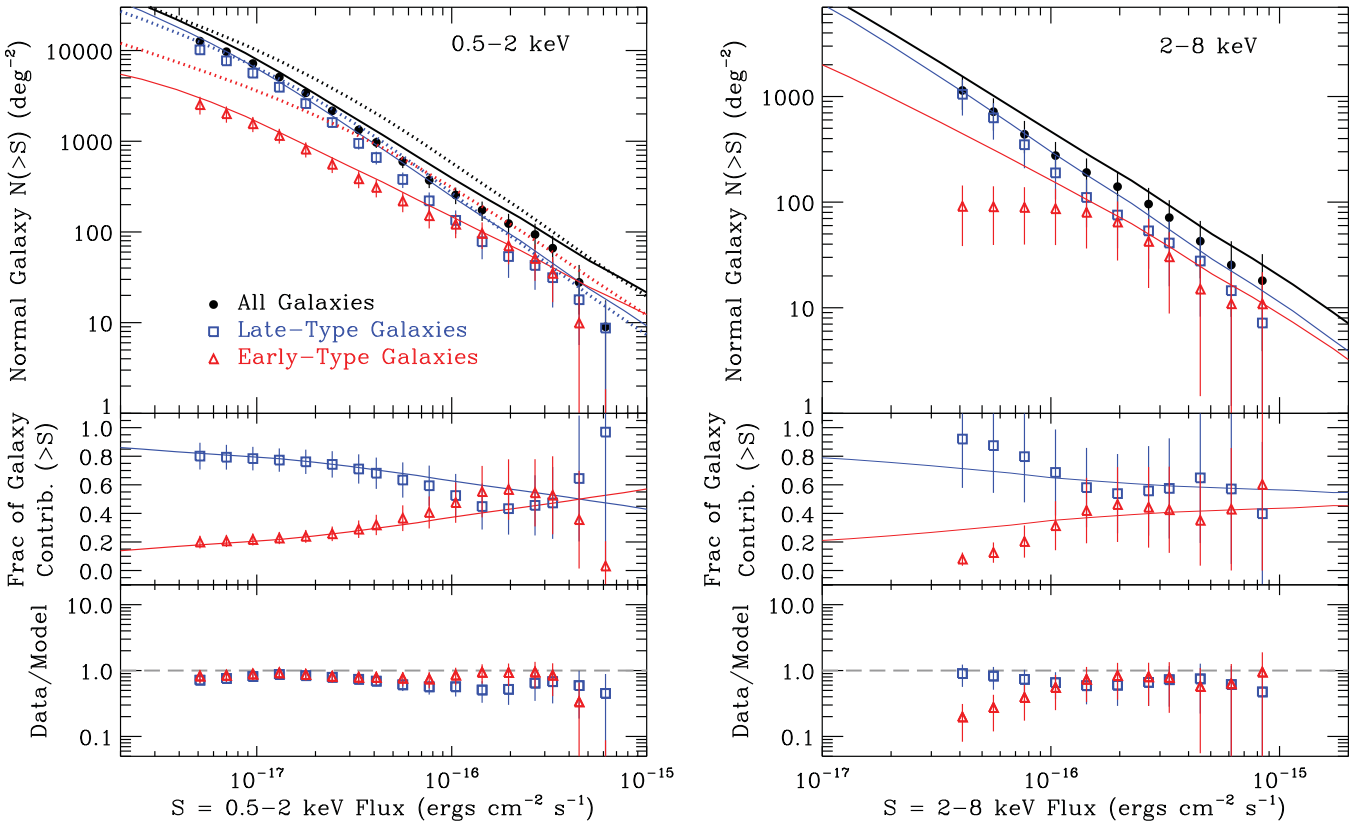

Figure 15. Top panels: similar to Figure 13, but for normal galaxies divided into late-type (open blue squares) and early-type (open red triangles) galaxy populations. The classification of galaxy morphology is explained in Section 3.3. The dotted curves in the upper-left panel show the predicted late-type (blue dotted curve) and early-type (red dotted curve) galaxy number counts based on the observed XLF pure-luminosity evolution parameterization derived by Ptak et al. (2007) using observed XLFs out to $z \approx 0.75$. These predictions are based on extrapolation of the XLF parameterization out to $z \approx 2$. The solid curves in the left and right panels show the predicted number counts for late-type (blue solid curve) and early-type (red solid curve) galaxy populations based on the observed mass functions converted to XLFs using X-ray scaling relations (see Section 4.2 for details). Middle panels: the fractional contributions that late-type and early-type galaxies make to the total galaxy population. Bottom panels: the ratio between the data and predictions based on the solid curves in the top panels. The reasonable agreement between the number-count data and models, both here and in Figure 13, indicates that the rapidly rising galaxy counts are largely attributed to the evolution of galaxy physical properties (e.g., stellar mass and star formation rate) with little redshift evolution in scaling relations between these physical properties and X-ray power output.

(A color version and a machine-readable table of the morphology-divided normal-galaxy cumulative number-count data for all four bandpasses of this figure are available in the online journal.)

similar results. When estimating galaxy number-count predictions, we used Equation (9) and extrapolated the Ptak et al. (2007) parameterizations out to $z \approx 2$. The Ptak et al. (2007) XLFs were directly measured for galaxies out to $z \approx 0.75$ (using galaxies with redshifts as large as $z \approx 1.2$) and are in good agreement with other galaxy XLF measurements from the literature (e.g., Norman et al. 2004; Tzanavaris & Georgantopoulos 2008). The uncertainties on the normalization of the XLF parameterization are a factor of ≈2. We find that, within the uncertainties, the XLFs provide reasonable predictions for the $z \lesssim 0.6$ (Figure 13, orange dotted curve and stars) and late-type galaxy (Figure 15, blue dotted curve and squares) number counts. For these two samples, the largest differences come from the $z \lesssim 0.6$ sample at 0.5–2 keV fluxes $\gtrsim 3 \times 10^{-17}$ erg cm^{-2} s^{-1}, which may be due to differences in galaxy classification of X-ray-detected sources, cosmic variance, and statistical errors associated with the XLF fits. We find that the extrapolated XLFs appear to overpredict the $z \gtrsim 0.6$ (Figure 13, green dotted curve and upside-down triangles) and early-type galaxy (Figure 15, red dotted curves and triangles) number counts by more than a factor of two, suggesting that our extrapolation of the early-type galaxy XLF evolution out to $z \approx 2$ is an overestimate. Therefore, it is possible that the *rate* by which the early-type galaxy XLF rises with redshift decreases somewhat going from $z \approx 0.75$ to 2 and/or the adopted rate of increase is too high (e.g., see Tzanavaris & Georgantopoulos 2008, who find a lower rate of increase). To obtain independent predictions of the galaxy XLFs and number counts for galaxies out to $z \approx 2$, we can use the combination of X-ray scaling relations (e.g., the X-ray/SFR relation) and the redshift evolution of galaxy physical properties (e.g., SFR and stellar mass) that are measured using multiwavelength observations.

Recent X-ray stacking investigations of large normal-galaxy populations selected by morphology and galaxy physical properties (e.g., SFR and stellar mass) have now provided insight into how the X-ray emission from normal galaxies evolves relative to galaxy physical properties out to $z \approx 1$–4. Lehmer et al. (2008) reported that late-type star-forming galaxies, the most numerous galaxy population in the universe, have mean L_X/SFR values that are roughly constant out to $z \approx 1.4$. Further X-ray stacking of distant $z \approx 1.5$–4 Lyman break galaxies appears to show similar mean L_X/SFR values (e.g., Brandt et al. 2001; Lehmer et al. 2005; Laird et al. 2006; Cowie et al. 2012; A. Basu-Zych et al. 2012, in preparation). Similarly, Vattakunnel et al. (2012) have studied $z \lesssim 1.2$ normal galaxies in the ≈4 Ms CDF-S at X-ray and radio wavelengths and found that the L_X–$L_{1.4\,GHz}$ correlation for these galaxies is consistent with that expected from the local L_X/SFR relation, albeit with significant scatter

(≈0.4 dex). Additional indirect support for a roughly constant L_X/SFR ratio with redshift has been provided by Dijkstra et al. (2012), who used the observed SFR density evolution of the universe to show that the unresolved SB CXRB can be fully explained by an L_X/SFR ratio $\propto(1+z)^b$, where b is constrained to be less than 1.4.

For early-type galaxies, Lehmer et al. (2007) and Danielson et al. (2012) showed that the SB X-ray luminosity per unit B-band luminosity (L_X/L_B) appears to undergo only mild evolution ($\propto(1+z)^{1.2}$) to $z \approx 1.2$ for the most optically luminous galaxies, which is expected to be due to X-ray-emitting hot gas. In contrast, however, lower-luminosity early-type galaxies have been found to have rising mean L_X/L_B values with increasing redshift, which is expected to be due to a fading LMXB population toward the present day (Lehmer et al. 2007; A. E. Hornschemeier et al. 2012, in preparation). Similar expectations have been found from X-ray binary population-synthesis models, which predict an evolution of $L_X/L_B \propto (1+z)^2$ at $z \lesssim 1$ (Fragos et al. 2012, in preparation; see also Ghosh & White 2001).

The above investigations provide estimates for how scaling relations between X-ray luminosity and galaxy physical properties have evolved out to $z \approx 1$–4, where the majority of the ≈4 Ms CDF-S normal galaxies are detected. It seems that only the scaling relation between LMXB emission and stellar mass undergoes significant evolution with cosmic time; however, these populations are expected to dominate only in early-type galaxies, which make up a minority of the X-ray-detected sources in the ≈4 Ms CDF-S. It is therefore likely that the evolving normal-galaxy XLF and rising galaxy number counts, observed here and in previous studies, are largely due to the rapid evolution of galaxy physical properties. Recent multiwavelength surveys (e.g., COSMOS; Scoville et al. 2007) have provided significant new constraints on the evolution of optical/near-IR luminosity, SFR, and stellar-mass functions. These measurements can be combined with scaling relations between X-ray luminosity and galaxy physical properties to make predictions for the evolution of the normal-galaxy XLFs and number counts for galaxies out to $z \approx 2$.

Following Avni & Tananbaum (1986), φ_X can be estimated through the following transformation:

$$\varphi_X(\log L_X, z) = \int_{-\infty}^{\infty} \varphi_\vartheta(\log\vartheta, z) P(\log L_X|\log\vartheta)\, d\log\vartheta, \tag{10}$$

where ϑ represents a galaxy physical property (e.g., optical luminosity, stellar mass, or SFR) by which $\varphi_\vartheta(\log\vartheta, z)$ has been measured, and $P(\log L_X|\log\vartheta)$ is the probability distribution for observing L_X given the value ϑ.

We make use of the redshift-dependent stellar-mass functions measured by Ilbert et al. (2010) for late-type and early-type galaxies out to $z \approx 2$ (i.e., $\vartheta = M_\star$). To convert $\varphi_{M_\star}(\log M_\star, z)$ to $\varphi_X(\log L_X, z)$ via Equation (9) requires knowledge of the transformation between X-ray luminosity and stellar mass (i.e., $P(\log L_X|\log M_\star)$). This function is expected to depend on galaxy morphology. In its most general form, we can express the transformation function as follows:

$$P(\log L_X|\log M_\star) = \frac{1}{\sqrt{2\pi}\sigma} \times \exp\left[-\frac{(\log L_{X,\rm mod}(M_\star) - \log L_X)^2}{2\sigma^2}\right], \tag{11}$$

where $L_{X,\rm mod}(M_\star)$ is the predicted X-ray luminosity given a value of the stellar mass $M_\star$ and σ represents the scatter in the relation. For normal late-type galaxies in the local universe, the X-ray luminosity has been shown to correlate strongly with SFR (e.g., Persic & Rephaeli 2007; Lehmer et al. 2010; Pereira-Santaella et al. 2011; Symeonidis et al. 2011; Mineo et al. 2012), and as discussed above, this correlation is observed to hold out to $z \gtrsim 1$. We made use of the Lehmer et al. (2010) X-ray/SFR relation for late-type star-forming galaxies in the local universe:

$$L_{2-10\,\rm keV} = \alpha M_\star + \beta \rm SFR, \tag{12}$$

where $\alpha = 9.08\times10^{28}$ erg s^{-1} $M_\odot^{-1}$ and $\beta = 1.62\times10^{39}$ erg s^{-1} $(M_\odot\ \rm yr^{-1})^{-1}$, $M_\star$ is in units of $M_\odot$, SFR is in units of $M_\odot$ yr^{-1}, and $L_{2-10\,\rm keV}$ is in units of erg s^{-1}. Studies of local and distant galaxy populations have shown that the SFR for late-type star-forming galaxies is further strongly correlated with $M_\star$ out to $z \approx 2$ (e.g., Daddi et al. 2007; Elbaz et al. 2007; Peng et al. 2010), albeit with a rapidly evolving normalization (i.e., mean SFR/$M_\star$) with redshift (e.g., Zheng et al. 2007; Karim et al. 2011; Cen 2011). To convert SFR to $M_\star$ for late-type star-forming galaxies, we adopted the relation provided by Karim et al. (2011):

$$\rm SFR/\mathit{M}_\star = \mathit{c}_0(1+\mathit{z})^{3.5}(\mathit{M}_\star/10^{11}\,\mathit{M}_\odot)^{\beta_{\rm SFR}}, \tag{13}$$

where $c_0 \approx 0.0263$ Gyr^{-1} and $\beta_{\rm SFR} \approx -0.4$ are fitting constants. Combining this relation with Equation (12), we arrive at the following expression:

$$L_{2-10\,\rm keV} = \alpha M_\star + \gamma(1+z)^{3.5} M_\star^{0.6}, \tag{14}$$

where $\gamma = 1.07\times10^{33}$, $M_\star$ is in units of $M_\odot$, and $L_{2-10\,\rm keV}$ is in units of erg s^{-1}. When computing number-count predictions, we converted the 2–10 keV luminosities provided here to other bandpasses assuming a power-law SED with $\Gamma = 1.9$, the average stacked SED of the X-ray-detected normal galaxies (Young et al. 2012). The overall scatter (accounting for both SFR/$M_\star$ and L_X/SFR relations) in this relation is estimated to be $\sigma \approx 0.4$ dex.

For normal early-type galaxies, the X-ray luminosity has been shown to correlate with K-band luminosity, L_K, which provides a direct proxy for galaxy stellar mass (e.g., Gilfanov 2004; Boroson et al. 2011). We converted the Boroson et al. (2011) L_X/L_K relations for early-type galaxies to $L_X/M_\star$ relations assuming a single mass-to-light ratio $\log M_\star/L_K \approx -0.2$ (where $M_\star$ and L_K are in solar units) characteristic of early-type galaxies. These relations are separated into contributions from LMXBs and hot X-ray-emitting gas:

$$\begin{aligned}\log L_{0.3-8\,\rm keV}(\rm LMXB) &\approx 29.2 + \log M_\star + 2\log(1+z)\\ \log L_{0.3-8\,\rm keV}(\rm gas) &\approx -6.07 + 4.03\log M_\star,\end{aligned} \tag{15}$$

where the $2\log(1+z)$ term accounts for the expected redshift evolution for LMXBs in early-type galaxies (see discussion above). When computing number-count predictions, we converted the 0.3–8 keV relations to other bandpasses assuming a power-law SED with $\Gamma = 1.8$ for LMXBs and an `apec` plasma model with an $L_{0.3-8\,\rm keV}$-dependent temperature ($T_X \propto L_{0.3-8\,\rm keV}^{0.21}$) and solar abundances for the hot gas. The scatter in the LMXB and hot-gas relations is estimated to be ≈0.2 dex and ≈1.0 dex, respectively (see Boroson et al. 2011).

The relations expressed in Equations (14) and (15), combined with the stellar-mass functions from Ilbert et al. (2010), were

folded into Equation (9) to obtain redshift-dependent XLFs for late-type and early-type galaxies, respectively. We measured the number counts of both populations in two redshift bins by integrating Equation (9) over the redshift intervals $z \lesssim 0.6$ and $z \gtrsim 0.6$ and summing the contributions from each galaxy morphology type. In Figures 13 and 15, we show our model number counts in bins of redshift and morphology, respectively, and in the bottom panels, we plot the ratio of our data to the model. We remind the reader that the models implemented here are not fits to the data in any way. For the redshift-divided normal-galaxy samples, we find good agreement between our data and the models at the SB and HB flux limits; however, for the number counts for normal galaxies at $z \gtrsim 0.6$, we find significant differences at the bright end ($f_{0.5-2\,\mathrm{keV}}$ and $f_{2-8\,\mathrm{keV}} \gtrsim 10^{-16}$ erg cm^{-2} s^{-1}). The bright-end number counts for $z \gtrsim 0.6$ galaxies are based on only ≈1–5 objects; therefore, the differences with the models may be due to either cosmic variance or misclassification of some fraction of these sources (i.e., if some of these normal galaxies are actually AGNs). Furthermore, the general trends seen in the data and models (e.g., the increasing contributions and faint-end dominance in the SB of $z \gtrsim 0.6$ galaxies) appear to be broadly consistent with each other. For the morphology-selected number counts, we find very good agreement (less than a factor of ≈1.5 difference) between the data and the model with the exception of the HB early-type galaxy counts. We note, however, that the HB number-count measurements for early-type galaxies are based on small numbers of galaxies (four galaxies) and are sensitive to the classifications discussed in Section 3.1 above.

In summary, we find that our models provide good characterizations of the X-ray number counts in redshift bins for both late-type and early-type galaxy populations down to the flux limits of our survey (with the exception of $z \gtrsim 0.6$ normal galaxies with bright SB and HB fluxes and HB early-type galaxy counts; however, see discussion above). For late-type galaxies, this result suggests that X-ray scaling relations in the local universe appear to hold out to at least $z \approx 1$–2, in agreement with previous investigations. For early-type galaxies, these results are consistent with there being little redshift evolution in how hot-gas X-ray emission scales with stellar mass and modest redshift evolution ($\propto(1+z)^2$) in the LMXB luminosity per stellar mass.

5. THE IMPENDING DOMINANCE OF NORMAL GALAXIES: PREDICTIONS FOR FUTURE DEEPER X-RAY OBSERVATIONS

The number-count results presented above show that normal galaxies play an increasingly dominant role in the extragalactic X-ray source population going to fainter fluxes. Our observations show that the cumulative SB and FB number counts of normal galaxies are on the brink of surpassing those of AGNs (see Figure 5), and the slope of the galaxy number counts (dN/dS) already exceeds that of AGNs (see Figure 6). At the SB flux limit of the ≈4 Ms CDF-S normal galaxies are reaching the unprecedented source density of ≈12,700 deg^{-2}, which constitutes ≈46% of the total number counts. Given the comparable source densities of normal galaxies and AGNs at the survey flux limit and the relatively sharp faint-end rise in the galaxy number counts versus AGNs ($N(>S)$ power-law slope of $\beta^{\mathrm{gal}} - 1 \approx 1.2$ versus $\beta_1^{\mathrm{AGN}} - 1 \approx 0.5$; see Table 1), it is clear that going to fainter *Chandra* fluxes beyond ≈4 Ms will yield larger gains in X-ray source densities than previous increases in depth. X11 showed that exposures of the CDF-S region will yield substantial gains in sensitivity. For example, a feasible ≈10 Ms exposure would permit a factor of ≈1.8 increase in depth (in terms of flux limit) over the current ≈4 Ms exposure. Therefore, exploring the normal-galaxy-dominated regime of the number-count distribution is a sensible goal that may be pursued in future surveys. At present, the only X-ray mission capable of reaching these fluxes is *Chandra* (see below), and this will likely be the case for at least the next two decades.

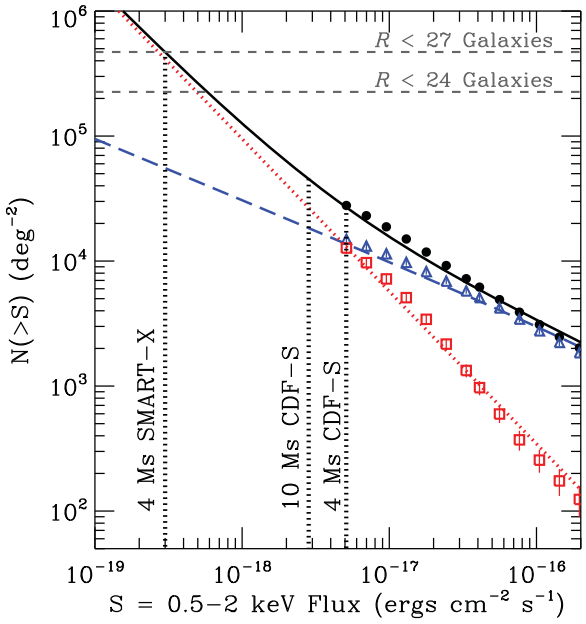

Figure 16. Measured SB number counts (filled black circles) with contributions from AGNs (open blue triangles) and normal galaxies (open red squares) shown. Our best-fit parameterizations from Equation (5) for all sources, AGNs, and normal galaxies have been shown as solid black, dashed blue, and dotted red curves, respectively. An extrapolation of these models indicates that the normal-galaxy number counts will overtake those of AGNs at SB flux levels of ≈(3–5) $\times 10^{-18}$ erg cm^{-2} s^{-1}. The ultimate flux limits of the ≈4 Ms CDF-S, a potential ≈10 Ms CDF-S, and future ≈4 Ms *SMART-X* exposures have been indicated. These extrapolations indicate that a ≈10 Ms CDF-S would have SB number counts at the flux limit that reach source densities of ≈46,000 deg^{-2} and are dominated by normal galaxies. More ambitiously, a ≈4 Ms *SMART-X* exposure would reach source densities of ≈500,000 deg^2 and would have a ≈90% contribution from normal galaxies. For reference, we have plotted the source densities of galaxies with *R*-band magnitudes brighter than $R \approx 24$ and $R \approx 27$ (gray short-dashed lines).

(A color version of this figure is available in the online journal.)

In Figure 16, we provide an expanded view of the SB number counts and their contributions by extragalactic source type (AGNs and normal galaxies) in the faint-flux regime. Our best-fit number-count parameterizations (based on Equation (5)) have been indicated. Direct extrapolation of these parameterizations indicates that the number counts of normal galaxies will overtake those of AGNs just below our current flux limit at ≈(3–5) $\times 10^{-18}$ erg cm^{-2} s^{-1}. With a ≈10 Ms exposure in the CDF-S, we could study number counts down to a sensitivity limit of ≈2.8×10^{-18} erg cm^{-2} s^{-1} (see vertical dotted line in Figure 16), although we expect that the faintest sources will have most probable fluxes of ≈5.2×10^{-18} erg cm^{-2} s^{-1} (see Section 2.1 for distinction). At such a depth, we would expect a factor of ≈1.7 increase in total X-ray source densities to ≈46,000 deg^{-2} (based on extrapolation of our best-fit number-count parameterization), with normal galaxies making up ≈57% of the limiting source density. After considering variations in sensitivity across the field, we expect that a 10 Ms exposure would yield ≈1020–1080 total X-ray-detected sources.

While *Chandra* is the only operating observatory capable of observing to the ultra-deep regime studied here, the realization of future X-ray mission concepts like *Generation-X* and *SMART-X*,[17] which have much larger light-collecting areas and comparable or improved imaging resolution over *Chandra*, would allow for the exploration of new populations of extragalactic X-ray sources, including new populations of distant ($z \gtrsim 0.6$) normal galaxies (see, e.g., Figure 13). Under its current specification, a ≈4 Ms *SMART-X* survey would detect SB sources with fluxes as low as $\approx 3 \times 10^{-19}$ erg cm^{-2} s^{-1}. Direct extrapolation of our number counts to these levels predicts source densities of ≈500,000 deg^{-2}, with ≈90% contribution from normal-galaxy populations.

6. SUMMARY

In this paper, we have provided new quantitative measurements of the X-ray number counts in the ≈4 Ms CDF-S using four bandpasses: 0.5–2 keV, 2–8 keV, 4–8 keV, and 0.5–8 keV (SB, HB, UHB, and FB, respectively). Our analyses focus on the faintest flux regimes only accessible by such ultra-deep *Chandra* surveys. We draw the following key conclusions:

1. We make use of a Bayesian approach, flux probability distributions, and maximum-likelihood techniques to measure number counts for sources detected in the ≈4 Ms CDF-S down to SB, HB, UHB, and FB flux limits of 5.1×10^{-18}, 3.7×10^{-17}, 4.6×10^{-17}, and 2.4×10^{-17} erg cm^{-2} s^{-1}, respectively; these are factors of ≈1.9–4.3 times fainter than previous number-count investigations.
2. At the flux limits of our survey, we reach source densities of 27,800, 10,500, 8400, and 22,600 deg^{-2} in the SB, HB, UHB, and FB, respectively. AGNs are the majority contributors to the total number counts at all fluxes in all four bands (especially in the HB and UHB). In the SB, we reach AGN sky densities of ≈14,900 deg^{-2}, the highest reliable AGN sky density measured at any wavelength.
3. The normal-galaxy number counts rapidly rise, compared with AGNs, and at the SB and FB flux limits, normal galaxies make up ≈46% and ≈43% of the number counts, respectively. At the limiting SB flux, normal galaxies reach a sky density of ≈12,700 deg^{-2}, which is a factor of ≈4.5 times higher than measured in the ≈2 Ms surveys.
4. Stated in terms of the intensity on the sky, X-ray-detected sources in the ≈4 Ms CDF-S can account for ≈76%–88% of the CXRB. We estimate that the increased exposure from ≈1–2 Ms to ≈4 Ms has resulted in an increase of ≈1%–2% resolved CXRB.
5. In the SB and HB, AGNs at high redshifts ($z \gtrsim 1.5$), with moderate to significant obscuration ($N_{\rm H} \gtrsim 10^{22}$ cm^{-2}), and relatively low intrinsic 0.5–8 keV luminosity ($L_{\rm X} \lesssim 10^{43}$ erg s^{-1}) make increasingly important contributions to the AGN number counts going to fainter fluxes, and at the flux limits, these sources make up ≳40% of the overall AGN number counts. These trends are broadly consistent with those expected from the phenomenological models of G07.
6. In the SB and HB, late-type star-forming galaxies with $z \lesssim 0.6$ provide majority contributions to the normal-galaxy number counts, with the exception of the SB counts below $\approx 10^{-17}$ erg cm^{-2} s^{-1}, where $z \gtrsim 0.6$ star-forming galaxies dominate. These galaxies are expected to produce X-ray emission from high- and low-mass X-ray binaries, hot gas, and young stars. By contrast, passive early-type galaxies, with X-ray emission produced by LMXBs and hot gas, make up only small fractions (≈5%–20%) of the SB and HB number counts near the survey flux limits. These trends are well described by models that assume that (1) the X-ray power output for late-type galaxies scales with SFR out to $z \approx 2$ with no evolution in the scaling relation and (2) the X-ray power output in early-type galaxies is due to a non-evolving hot-gas-emitting component and an evolving (by $(1+z)^2$) LMXB component that both scale with stellar mass. Therefore, the rapidly rising normal-galaxy number counts can be attributed primarily to the evolution of the physical properties of galaxies (i.e., SFR and stellar mass) and not X-ray scaling relations.
7. Extrapolation of our number counts to lower fluxes suggests that an X-ray observation reaching flux levels just below those probed by the ≈4 Ms CDF-S (at SB fluxes of $\approx (3\text{–}5) \times 10^{-18}$ erg cm^{-2} s^{-1}) would result in an X-ray sky with normal galaxies dominating the source density at the sensitivity limit. Since the normal-galaxy number counts are now comparable with AGNs at the ≈4 Ms flux limit and are expected to continue to rise rapidly at fainter fluxes, more sensitive surveys will have relatively large yields in increased source densities. We show that a 10 Ms CDF-S would yield ≈1020–1080 total sources and would result in a limiting SB source density of ≈46,000 deg^{-2} with normal galaxies dominating the number counts (providing ≈57% of the total number counts) at the flux limit.

We thank the anonymous referee for reviewing the manuscript and providing useful suggestions. We thank Andy Fabian for useful discussions and acknowledge James Aird, Hermann Brunner, Fabrizio Fiore, Simonetta Puccetti, and Shaji Vattakunnel for sharing data; these contributions have helped the quality of this paper. We gratefully acknowledge financial support from the Einstein Fellowship Program (B.D.L.), CXC grant SP1-12007A and NASA ADP grant NNX10AC99G (Y.Q.X. and W.N.B.), the Science and Technology Facilities Council (D.M.A.), Financiamento Basal, CONICYT-Chile FONDECYT 1101024 and FONDAP-CATA 15010003, and CXC grant SAO SP1-12007B (F.E.B.), and ASI-INAF grants I/088/06 and I/009/10/0 (A.C., R.G., C.V.).

APPENDIX

RECOVERY FRACTION CORRECTIONS

As noted in Section 2.2, the X11 CDF-S source catalog was generated following a two-step approach, which entailed (1) running `wavdetect` to form an initial list of candidate sources and (2) assessing the probability of detection using `AE`. Our methods described in Section 2 for computing number counts generally account for biases due to completeness and the Eddington bias provided that our catalogs are complete to a specific `AE` source selection probability. Therefore, we need to account for incompletenesses in the number counts that result as a consequence of our two-step cataloging approach. In this section, we summarize our approach for computing this correction, which has been implemented in Equation (5) as the quantity C'.

We began by generating 200 mock CDF-S images in the four bandpasses (i.e., 800 images), which each contained 700 X-ray

[17] See http://www.cfa.harvard.edu/hea/genx/ and http://hea-www.cfa.harvard.edu/SMARTX/ for more information about *Generation-X* and *SMART-X*, respectively.

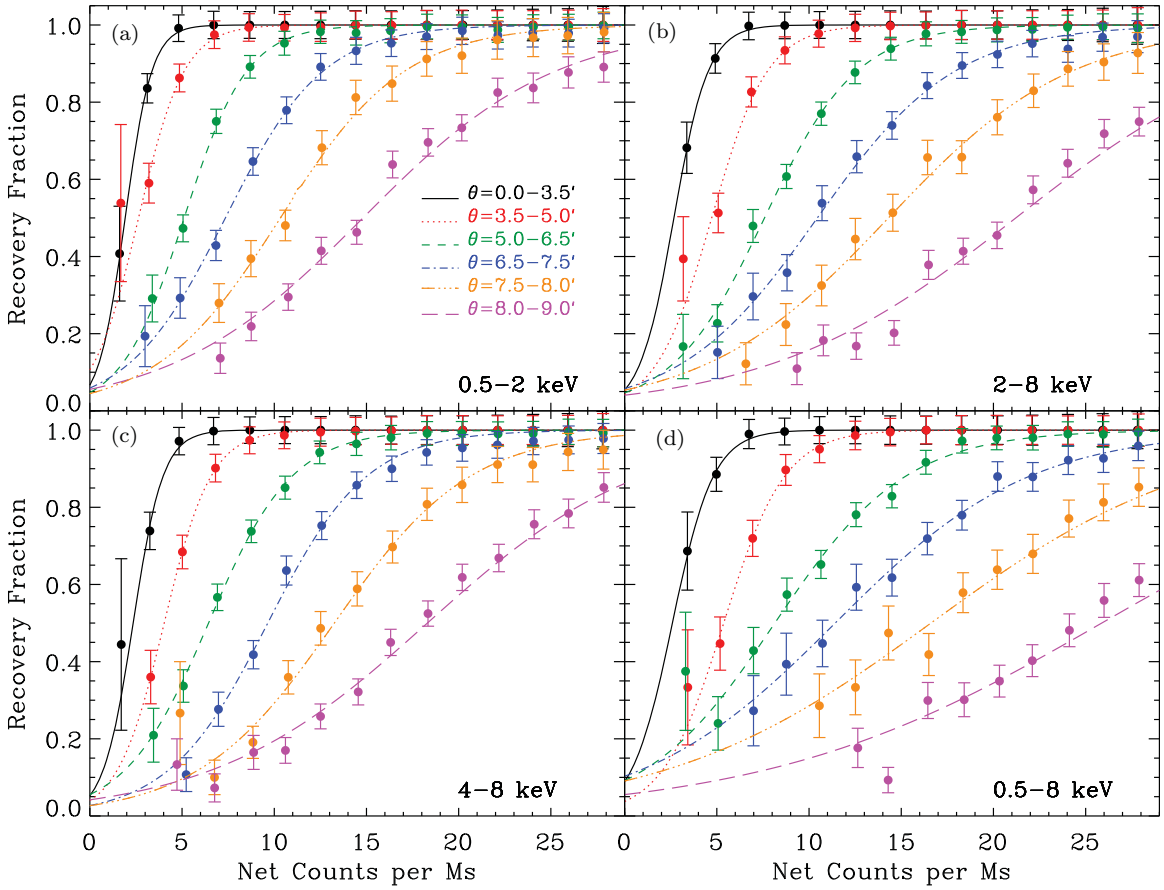

Figure 17. Fraction of simulated sources satisfying the binomial probability selection criterion of Equation (1) that were also detected using `wavdetect` at a false-positive probability threshold of 10^{-5} (i.e., $f_{\rm recov}$; filled circles with error bars) for the four bandpasses. Each color represents a different off-axis angle interval as annotated on the plot. Our best-fit models, as described in the Appendix, have been plotted as curves (see annotation); these models have been used to correct for incompleteness in our number-count computations in Section 2.

(A color version of this figure is available in the online journal.)

sources artificially implanted. These images were constructed as follows. Each source was assigned a random right ascension and declination within the area of the ≈4 Ms CDF-S as defined by the exposure maps (see Section 3 of X11) and was given a random number of counts between ≈1 and 100. The counts from each source were added to a blank image canvas using the `marx`[18] (version 4.5) ray-tracing code. In this procedure, the PSF of each source was modeled assuming a roll angle and aim point that were selected from one of the 54 observations that make up the cumulative ≈4 Ms CDF-S exposure (see Table 1 of X11). Selection of the roll angle and aim point for each source was done probabilistically with the probability of selection being directly proportional to the exposure time of each of the 54 CDF-S observations. Mock images for each of the four bandpasses were then created by adding background counts from the respective cumulative background images (see Section 7.1 of X11) to the image canvases.

For each of the 700 sources in each of the 800 images we performed circular aperture photometry using a circular aperture with a radius encompassing ≈90% of the EEF. The number of counts measured for each source was then compared with the number of counts needed for a source detection (see discussion of sensitivity maps in Section 2.1) to see if it would satisfy the criterion adopted in Equation (1) for source detection. We then searched each of the 800 images using `wavdetect` at a false-positive probability threshold of 10^{-5} and made `wavdetect` source catalogs for each image. For each bandpass, we combined all 200 catalogs of 700 sources and computed the count rate ϕ and off-axis angle θ-dependent fraction of sources that satisfied our binomial probability selection criterion (i.e., Equation (1)) that were also detected by `wavdetect` (hereafter recovery fraction $f_{\rm recov} \equiv 1/C'$).

In Figure 17, we show the $f_{\rm recov}$ versus ϕ for off-axis angle intervals going to $\theta \approx 9$ arcmin, where the image is roughly radially contiguous. We found that the data for $f_{\rm recov}$ could be represented successfully using the analytic form $f_{\rm recov}(\phi, \theta) = 1/(1 + \exp[-\delta(\theta)\{\phi - \xi(\theta)\}])$, where $\delta(\theta)$ and $\xi(\theta)$ are fitting constants that vary with off-axis angle and bandpass. In Section 2.2, we made use of this relation in Equation (6), where we adopt $C' = 1/f_{\rm recov}$. We note that this correction has the advantage in that it is independent of the Bayesian priors discussed in Section 2 and does not depend on the shape of the number-count distribution near and below the flux limits.

[18] See http://space.mit.edu/cxc/marx/ for `marx` simulator details.

REFERENCES

Aird, J., Nandra, K., Laird, E. S., et al. 2010, MNRAS, 401, 2531
Alexander, D. M., Bauer, F. E., Brandt, W. N., et al. 2003, AJ, 126, 539
Arnaud, K. A. 1996, in ASP Conf. Ser. 101, Astronomical Data Analysis Software and Systems V, ed. G. H. Jacoby & J. Barnes (San Francisco, CA: ASP), 17
Avni, Y., & Tananbaum, H. 1986, ApJ, 305, 83

Bauer, F. E., Alexander, D. M., Brandt, W. N., et al. 2002, AJ, 124, 2351
Bauer, F. E., Alexander, D. M., Brandt, W. N., et al. 2004, AJ, 128, 2048 (B04)
Bell, E. F., Wolf, C., Meisenheimer, K., et al. 2004, ApJ, 608, 752
Boroson, B., Kim, D.-W., & Fabbiano, G. 2011, ApJ, 729, 12
Brandt, W. N., & Alexander, D. M. 2010, Proc. Natl Acad. Sci., 107, 7184
Brandt, W. N., Alexander, D. M., Hornschemeier, A. E., et al. 2001, AJ, 122, 2810
Brandt, W. N., & Hasinger, G. 2005, ARA&A, 43, 827
Broos, P. S., Townsley, L. K., Feigelson, E. D., et al. 2010, ApJ, 714, 1582
Brunner, H., Cappelluti, N., Hasinger, G., et al. 2008, A&A, 479, 283
Brusa, M., Comastri, A., Gilli, R., et al. 2009, ApJ, 693, 8
Caldwell, J. A. R., McIntosh, D. H., Rix, H.-W., et al. 2008, ApJS, 174, 136
Cappelluti, N., Brusa, M., Hasinger, G., et al. 2009, A&A, 497, 635
Cardamone, C. N., van Dokkum, P. G., Urry, C. M., et al. 2010, ApJS, 189, 270
Cen, R. 2011, ApJ, 741, 99
Civano, F., Brusa, M., Comastri, A., et al. 2011, ApJ, 741, 91
Colbert, E. J. M., Heckman, T. M., Ptak, A. F., Strickland, D. K., & Weaver, K. A. 2004, ApJ, 602, 231
Cowie, L. L., Barger, A. J., Bautz, M. W., Brandt, W. N., & Garmire, G. P. 2003, ApJ, 584, L57
Cowie, L. L., Barger, A. J., & Hasinger, G. 2012, ApJ, 748, 50
Daddi, E., Dickinson, M., Morrison, G., et al. 2007, ApJ, 670, 156
Danielson, A. L. R., Lehmer, B. D., Alexander, D. M., et al. 2012, MNRAS, 422, 494
De Luca, A., & Molendi, S. 2004, A&A, 419, 837
Dijkstra, M., Gilfanov, M., Loeb, A., & Sunyaev, R. 2012, MNRAS, 421, 213
Draper, A. R., & Ballantyne, D. R. 2009, ApJ, 707, 778
Ebrero, J., Carrera, F. J., Page, M. J., et al. 2009, A&A, 493, 55
Elbaz, D., Daddi, E., Le Borgne, D., et al. 2007, A&A, 468, 33
Elvis, M., Civano, F., Vignali, C., et al. 2009, ApJS, 184, 158
Fabbiano, G. 1989, ARA&A, 27, 87
Fabbiano, G. 2006, ARA&A, 44, 323
Fiore, F., Puccetti, S., & Mathur, S. 2012, Adv. Astron., 2012, 271502
Freeman, P. E., Kashyap, V., Rosner, R., & Lamb, D. Q. 2002, ApJS, 138, 185
Georgakakis, A., Nandra, K., Laird, E. S., Aird, J., & Trichas, M. 2008, MNRAS, 388, 1205 (G08)
Georgakakis, A., Rowan-Robinson, M., Babbedge, T. S. R., & Georgantopoulos, I. 2007, MNRAS, 377, 203
Georgakakis, A. E., Chavushyan, V., Plionis, M., et al. 2006, MNRAS, 367, 1017
Ghosh, P., & White, N. E. 2001, ApJ, 559, L97
Giacconi, R., Rosati, P., Tozzi, P., et al. 2001, ApJ, 551, 624
Giacconi, R., Zirm, A., Wang, J., et al. 2002, ApJS, 139, 369
Gilfanov, M. 2004, MNRAS, 349, 146
Gilli, R., Comastri, A., & Hasinger, G. 2007, A&A, 463, 79 (G07)
Green, P. J., Silverman, J. D., Cameron, R. A., et al. 2004, ApJS, 150, 4
Hasinger, G., Miyaji, T., & Schmidt, M. 2005, A&A, 441, 417
Hickox, R. C., & Markevitch, M. 2006, ApJ, 645, 95
Hornschemeier, A. E., Bauer, F. E., Alexander, D. M., et al. 2003, AJ, 126, 575
Ilbert, O., Salvato, M., Le Floc'h, E., et al. 2010, ApJ, 709, 644
Iwasawa, K., Sanders, D. B., Evans, A. S., et al. 2009, ApJ, 695, L103
Iwasawa, K., Sanders, D. B., Teng, S. H., et al. 2011, A&A, 529, A106
Karim, A., Schinnerer, E., Martínez-Sansigre, A., et al. 2011, ApJ, 730, 61
Kim, D.-W., Barkhouse, W. A., Romero-Colmenero, E., et al. 2006, ApJ, 644, 829
Kim, D.-W., Cameron, R. A., Drake, J. J., et al. 2004a, ApJS, 150, 19
Kim, D.-W., Wilkes, B. J., Green, P. J., et al. 2004b, ApJ, 600, 59
Kim, M., Wilkes, B. J., Kim, D.-W., et al. 2007, ApJ, 659, 29
Laird, E. S., Nandra, K., Hobbs, A., & Steidel, C. C. 2006, MNRAS, 373, 217
Lehmer, B. D., Alexander, D. M., Bauer, F. E., et al. 2010, ApJ, 724, 559
Lehmer, B. D., Brandt, W. N., Alexander, D. M., et al. 2005, AJ, 129, 1
Lehmer, B. D., Brandt, W. N., Alexander, D. M., et al. 2007, ApJ, 657, 681
Lehmer, B. D., Brandt, W. N., Alexander, D. M., et al. 2008, ApJ, 681, 1163
Luo, B., Bauer, F. E., Brandt, W. N., et al. 2008, ApJS, 179, 19 (L08)
Luo, B., Brandt, W. N., Xue, Y. Q., et al. 2010, ApJS, 187, 560
Lusso, E., Comastri, A., Vignali, C., et al. 2011, A&A, 534, A110
Mateos, S., Warwick, R. S., Carrera, F. J., et al. 2008, A&A, 492, 51
Mignoli, M., Cimatti, A., Zamorani, G., et al. 2005, A&A, 437, 883
Mineo, S., Gilfanov, M., & Sunyaev, R. 2012, MNRAS, 419, 2095
Miyaji, T., & Griffiths, R. E. 2002, ApJ, 564, L5
Moretti, A., Campana, S., Lazzati, D., & Tagliaferri, G. 2003, ApJ, 588, 696
Moretti, A., Pagani, C., Cusumano, G., et al. 2009, A&A, 493, 501
Murphy, K. D., & Yaqoob, T. 2009, MNRAS, 397, 1549
Nevalainen, J., David, L., & Guainazzi, M. 2010, A&A, 523, A22
Norman, C., Ptak, A., Hornschemeier, A., et al. 2004, ApJ, 607, 721
O'Sullivan, E., Forbes, D. A., & Ponman, T. J. 2001, MNRAS, 328, 461
Peng, Y.-j., Lilly, S. J., Kovač, K., et al. 2010, ApJ, 721, 193
Pereira-Santaella, M., Alonso-Herrero, A., Santos-Lleo, M., et al. 2011, A&A, 535, A93
Persic, M., & Rephaeli, Y. 2007, A&A, 463, 481
Ptak, A., Mobasher, B., Hornschemeier, A., Bauer, F., & Norman, C. 2007, ApJ, 667, 826
Puccetti, S., Vignali, C., Cappelluti, N., et al. 2009, ApJS, 185, 586
Ranalli, P., Comastri, A., & Setti, G. 2003, A&A, 399, 39
Ranalli, P., Comastri, A., & Setti, G. 2005, A&A, 440, 23
Rosati, P., Tozzi, P., Giacconi, R., et al. 2002, ApJ, 566, 667
Schmidt, M., Schneider, D. P., & Gunn, J. E. 1995, AJ, 110, 68
Scoville, N., Aussel, H., Brusa, M., et al. 2007, ApJS, 172, 1
Silverman, J. D., Green, P. J., Barkhouse, W. A., et al. 2008, ApJ, 679, 118
Silverman, J. D., Mainieri, V., Salvato, M., et al. 2010, ApJS, 191, 124
Spergel, D. N., Verde, L., Peiris, H. V., et al. 2003, ApJS, 148, 175
Stark, A. A., Gammie, C. F., Wilson, R. W., et al. 1992, ApJS, 79, 77
Symeonidis, M., Georgakakis, A., Seymour, N., et al. 2011, MNRAS, 417, 2239
Szokoly, G. P., Bergeron, J., Hasinger, G., et al. 2004, ApJS, 155, 271
Tozzi, P., Gilli, R., Mainieri, V., et al. 2006, A&A, 451, 457
Treister, E., Urry, C. M., & Virani, S. 2009, ApJ, 696, 110
Tzanavaris, P., & Georgantopoulos, I. 2008, A&A, 480, 663
Ueda, Y., Akiyama, M., Ohta, K., & Miyaji, T. 2003, ApJ, 598, 886
Vattakunnel, S., Tozzi, P., Matteucci, F., et al. 2012, MNRAS, 420, 2190
Worsley, M. A., Fabian, A. C., Bauer, F. E., et al. 2005, MNRAS, 357, 1281
Xue, Y. Q., Brandt, W. N., Luo, B., et al. 2010, ApJ, 720, 368
Xue, Y. Q., Luo, B., Brandt, W. N., et al. 2011, ApJS, 195, 10 (X11)
Young, M., Brandt, W. N., Xue, Y. Q., et al. 2012, ApJ, 748, 124
Zheng, X. Z., Bell, E. F., Papovich, C., et al. 2007, ApJ, 661, L41